DOE Award #: DE-SC0008148

Awarded to: Case Western Reserve University

Project title: Mapping Interactions in Hybrid Systems with Active Scanning Probes

PI: Jesse Berezovsky

Date of report: Sept. 30, 2017

Date covered by report: July 1, 2012 – June 30, 2017

Description of accomplishments:

This project aimed to study and map interactions between components of hybrid nanodevices using a novel scanning probe approach. To enable this work, we initially constructed a flexible experimental apparatus allowing for simultaneous scanning probe and confocal optical microscopy measurements. This setup was first used for all-optical measurements of nanostructures, with the focus then shifting to hybrid devices in which single coherent electron spins are coupled to micron-scale ferromagnetic elements, which may prove useful for addressing single spins, enhanced sensing, or spin-wave-mediated coupling of spins for quantum information applications. A significant breakthrough was the realization that it is not necessary to fabricate a magnetic structure on a scanning probe – instead a ferromagnetic vortex core can act as an integrated, solid state, scanning probe. The core of the vortex produces a very strong, localized fringe field which can be used analogously to an MFM tip. Unlike a traditional MFM tip, however, the vortex core is scanned within an integrated device (eliminating drift), and can be moved on vastly faster timescales. This approach allows the detailed investigation of interactions between single spins and complex driven ferromagnetic dynamics.

1. Optical spectroscopy of quantum dots at room temperature

We have used the optical spectroscopy capabilities of our scanning probe/optical microscopy system to measure photoluminescence (PL) dynamics of individual semiconductor nanocrystal quantum dots (NCQDs). Because these materials provide a flexible platform for controllable, room-temperature confinement of individual electrons, they are of significant interest for opto-electronics and photovoltaics. One of the significant advantages of the spectroscopy system constructed at the beginning of this project is that the pulsed excitation source can be automatically tuned in both energy and power. (This is accomplished by using a broad-spectrum supercontinuum pulsed light source, in addition to several motorized, graded neutral density and edge pass filters). This allows us to vary excitation energy and intensity while studying single quantum dots. This differs from previous experiments, which typically did not have the capability to scan the excitation

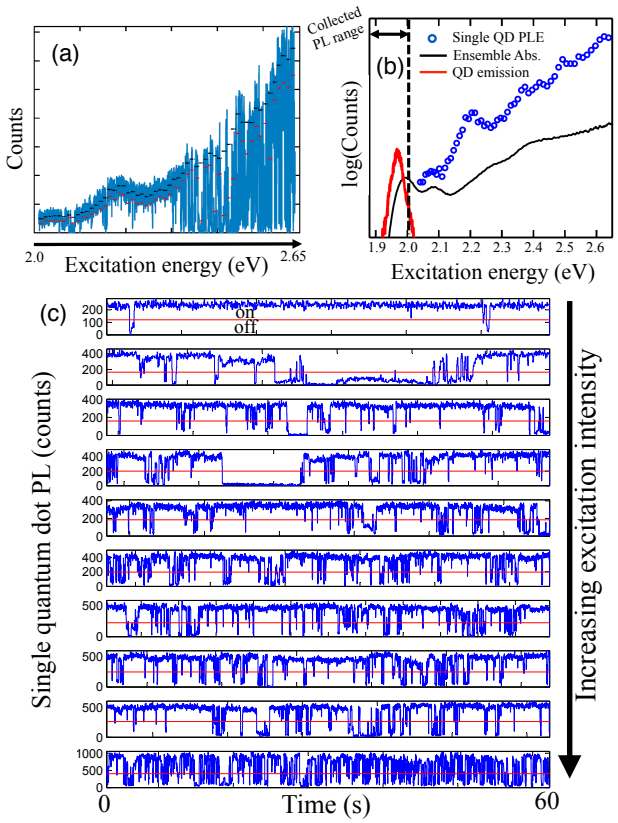

Figure 1. (a) PL counts vs. excitation energy for a single nanocrystal quantum dot. (b) PL-excitation spectrum for a single QD, compared to ensemble absorption spectrum. (c) Single quantum dot blinking at increasing excitation intensity.

energy continuously, and only compared different nanostructures under different conditions, not the same nanostructure under varying conditions.

By sweeping excitation energy and measuring emission from an individual NCQD, we gain information about the optical transition energies and their linewidths in these nanostructures [1,2]. Furthermore, by repeating this measurement on a number of NCQDs, we can learn about the dot-to-dot variation in these quantities. Figure 1a shows typical data from this photoluminescence excitation measurement. As the excitation energy is swept, the emission intensity changes in a non-monotonic fashion. (Changes in the blinking rate are also visible here.) When we extract emission intensity vs. excitation energy we can observe several peaks that are obscured in ensemble absorption measurements (Fig. 1b). We have analyzed the positions and widths of these peaks in approximately 40 quantum dots. By comparing the energies of the peaks to effective mass calculations, we can understand the electronic states involved in these transitions. We find that the broadening of these transitions arises from thermal broadening and from spectral diffusion due to the time-dependent variations in the local charge environment. The dot-to-dot variation in transition energy is caused by the quantum dot size and shape inhomogeneity within the ensemble. Interestingly, we have found that the strength of these mechanisms is not the same for different transitions, nor is it even monotonically increasing with energy. Instead, it depends on the sensitivity of the transition energy to changes in the confining potential, which depends on the details of the quantum size levels involved in the transition.

We have used the ability to sweep excitation intensity while monitoring single quantum dot emission to study the PL intermittency (blinking) vs. excitation rate. This effect can be seen in Fig. 1c, where as the excitation intensity is increased (and also the excitation rate), the emission turns on and off more rapidly. The blinking effect has been ascribed to charging and uncharging of the NCQD, which occurs as the local electrostatic environment fluctuates. The times between blinking events show power law statistics with an exponential cut-off, which can be

understood using a model of reaction rate kinetics. These models depend on several parameters, such as the energy of defect trap states, which are not well understood. By measuring blinking statistics vs. excitation rate, we can obtain a measurement of these parameters in an individual quantum dot. This measurement has been repeated on approximately 100 quantum dots yielding the mean and typical distribution of these parameters of interest.

We have also studied the coupling of quantum dots to a plasmonic nanocavity, in collaboration with the Strangi group at CWRU [3]. In this work, hollow metal nanopillars are fabricated, and with integrated nanocrystal quantum dots. We found that the excitons in the quantum dots couple to the plasmonic resonances in a novel way, resulting not in the expected amplified stimulated emission, but in an enhanced spontaneous emission. This is manifested by a reduced emission lifetime, in the absence of linewidth narrowing. Such an effect may find application for switchable photonic devices.

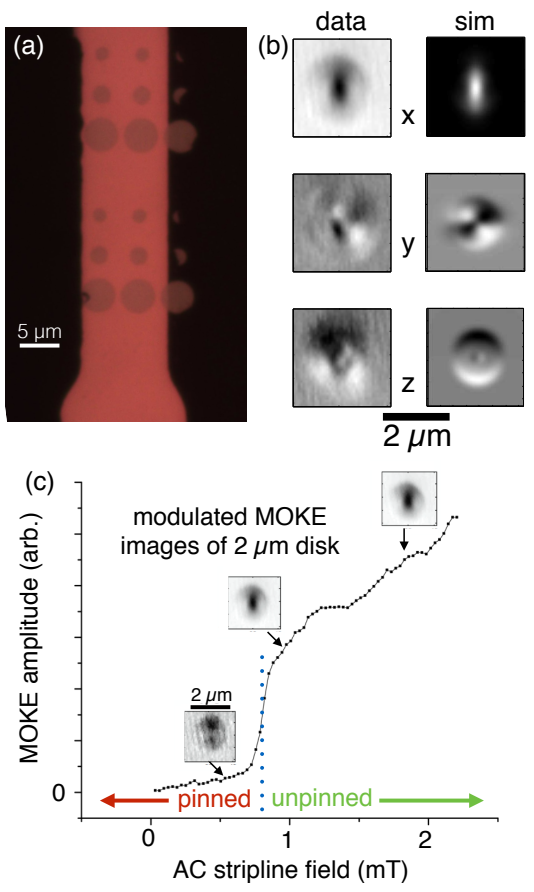

Figure 2. (a) Optical micrograph of permalloy disks on a stripline. (b) Map of 3-D magnetization response of a 2μm disk to an AC magnetic field in the *y*-direction. (c) Amplitude of central *x*-component signal vs. AC field strength. Insets show magnetization response map at selected driving voltages.

2. Mapping magnetization dynamics in driven micromagnets

A major achievement in this project was the development of a straightforward, highly sensitive technique for mapping the response of domain structure in micromagnets to an applied AC magnetic field [4]. This was critical for the ultimate plan of studying coupling of these driven micromagnets to confined spins. We have fabricated micron and sub-micron ferromagnetic disks and squares atop a metal stripline (see Fig. 2a). These structures display vortex-like domain structure. We have developed a scanning microscopy technique to probe the response of the magnetization to a driving field from DC to GHz frequencies. This is accomplished by using an amplitude-modulated driving field, and probing the samples using a laser that is also modulated. The laser is focused on the sample with an oil-immersion objective, and the sample is scanned with a nano-positioning stage, resulting in spatial resolution of approximately 300 nm. Typical data is shown in Fig. 2b. These experiments have uncovered new behavior of the magnetization dynamics

in these structures.

An important factor in magnetization dynamics is the tendency for a domain wall or vortex core to be pinned at defects. Instead of translating the vortex continuously, an applied field causes the vortex core to jump from one pinning site to another. The standard assumption is that the magnetic texture is completely rigid while pinned between jumps. Our dynamic differential probing technique results in a very sensitive measurement of the magnetization, and reveals the response of the magnetization while a vortex core is pinned. Away from the core, we see a rotation of the in-plane magnetization. We also observe a tilting of the out-of-plane core magnetization while it is pinned.

Our measurements have also allowed us to map out the pinning dynamics as the vortex is translated across the sample. As we increase the strength of the driving magnetic field, we see a strongly nonlinear response in the measured images (Fig. 2c), with a sudden jump corresponding to the depinning of the vortex core. As we translate the vortex with a bias magnetic field, we can observe the vortex core switching from one pinning site to the next, and measure the pinning strength. Additionally, we have been able to measure the effects of thermal fluctuations on the depinning process. By pushing the system close to a depinning transition, and varying the dwell time under those conditions, we can measure the probability for a thermally-activated depinning transition to occur. These results are of key importance in studying and controlling interactions between these systems and confined spins.

3. Imaging the pinning potential for ferromagnetic vortices

The sensitive magneto-optical microscopy technique described above was extended into a method for mapping the effective pinning potential through which a vortex core moves [5]. While sweeping the amplitude of an applied AC magnetic field up and down, we can measure the resulting displacement of the vortex core. We see multiple pinning and depinning events, as well as hysteresis in the different sweep directions. Fig. 3(a) shows two examples of hysteresis loops with AC field in the *y*-direction, and with different static magnetic fields in the *x*-direction. By identifying the endpoints of the pinned regions on these plots, we can extract an effective 1-D vortex pinning potential. Previously this type of hysteresis has only been observed at low temperature using a complicated micromechanical technique. Here, we are able to see the same thing at room temperature due the faster effective measurement time in our AC technique. The increased speed and simplicity of our technique allows us to repeat these measurements at many values of a static magnetic field, thereby raster scanning the vortex across the disk, mapping out successive lines of the pinning potential as we go. Fig. 3(b) shows such a map of the vortex pinning potential in the central region of a 2-μm-diameter, 30-nm-thick Permalloy disk. Each line is an effective 1-D pinning potential along the *x*-direction extracted from a hysteresis loop at a different static field used to sweep the vortex in the *y*-direction. The most surprising result is that instead of just individual localized pinning “sites,” we also see extended lines of pinning. This suggests that the pinning

occurs at grain boundaries, overturning the typical zero-dimensional picture of pinning in these materials.

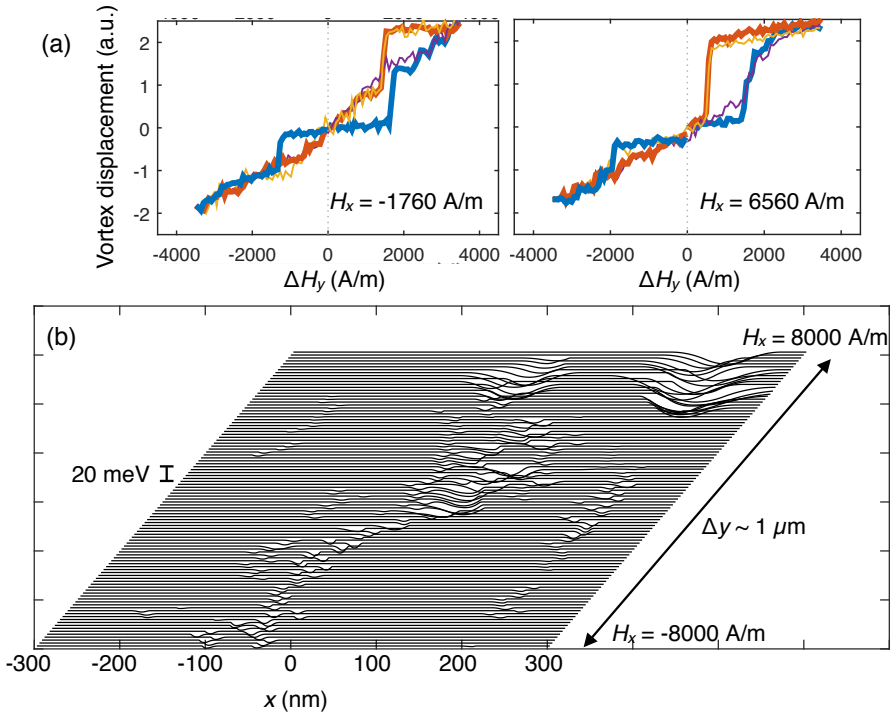

Figure 3. (a) Two examples of vortex displacement vs. AC magnetic field in the *y*-direction with a static field in the *x*-direction, showing pinning events and hysteresis. (b) Map of vortex pinning potential extracted from a series of hysteresis loops as in (a).

4. Coupling vortex scanning probe to single NV spins

With the vortex pinning potential mapped, we can then study coupling of the scanned ferromagnetic vortex to individual nitrogen-vacancy (NV) spins in diamond. In order to take full advantage of the nanoscale size of NVs for sensing applications, or to couple two NV spins via their dipole-dipole interaction, we need to be able to address and control NV spins separated by distances ~10 nm. The coupled NV/vortex system appears to be a promising avenue to achieve this, in a room temperature, integrated platform. Our results indicate that this hybrid system presents new intriguing physics, as the individual spin interacts with the mesoscopic, dynamic spin texture of the vortex.

Fig. 4a shows the concept of the coupled NV/vortex platform. The grayscale image shows a simulation of the out-of-plane magnetization of the vortex core. The arrows indicate the resulting simulated fringe field 20 nm above the surface of the magnetic disk (on a logarithmic scale). We then place a diamond nanoparticle, which contains several NVs within the particle's ~25 nm diameter, atop the disk. Using small magnetic fields, we then scan the vortex core across the disk. When the vortex core approaches the NVs, they experience a strong interaction with the vortex. Figure 4b shows the experimental realization of this platform, with the permalloy disk visible as the outlined blue circle, and the fluorescence from the NVs

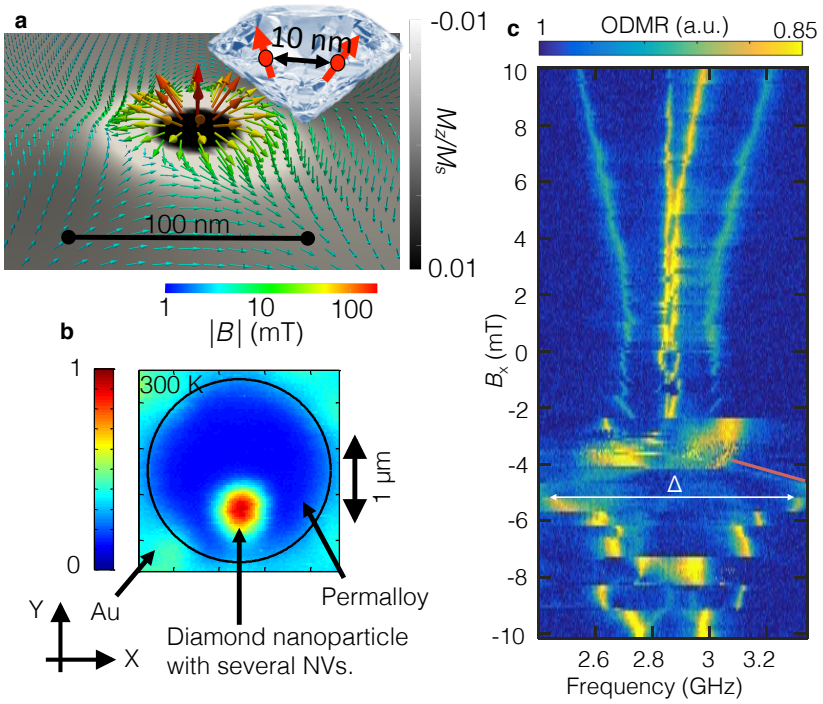

Figure 4. Coupling NV spins to a ferromagnetic vortex. (a) Simulation of vortex core out-of-plane magnetization (grayscale), and magnetic field 20 nm above surface (arrows). A diamond nanoparticle is then placed atop this structure. (b) Photoluminescence scan showing a Permalloy disk in a vortex state, with a diamond nanoparticle containing several NVs on top. (c) NV spin resonances vs. applied field. As the applied field drives the vortex near the NVs, large splitting Δ is observed, and large magnetic field gradient (red line).

in the nanoparticle showing up as the bright red spot. We then perform optically-detected magnetic resonance (ODMR) and magneto-optical microscopy measurements to map both the NV spin resonances and the vortex behavior [6].

Fig. 4c shows the rich interaction between the vortex and the NV spin transitions (revealed by the yellow lines in this ODMR data). At zero applied field, the vortex sits at the center of the disk. As the field is increased in the positive direction, the vortex moves away from the NVs and the spin splitting increases with field, as is typically observed. On the other hand, when the field is increased in the negative direction, the vortex core approaches the NVs, and more complex behavior in the spin transitions is seen resulting in large splitting, and large magnetic field gradients when the vortex makes its closest approach past the NVs (around $B_x = -5$ mT).

We have found that the coupling of the vortex to NV spins uncovers interesting physics beyond the large, local fringe field from the vortex core. A particularly rich facet of this system arises because the vortex as well as the NV spin can be driven dynamically by a microwave field, and the two then have a dynamic interaction with each other [7]. In the confined geometry of the permalloy disk, spin wave excitations have a discrete spectrum of modes. When a microwave field is applied, these spin wave modes can be excited. These modes then emit some pattern of microwaves, which can drive transitions in a nearby NV. We have measured this effect, by studying coherent Rabi oscillations between spin levels in a single NV, as a function of the relative position of the vortex core. Rabi data for the two spin transitions in a single NV are shown in Fig. 5a. All conditions other than the microwave frequency are the same, yet the two traces show dramatically different Rabi frequency. Further, both Rabi frequencies are higher than would be expected

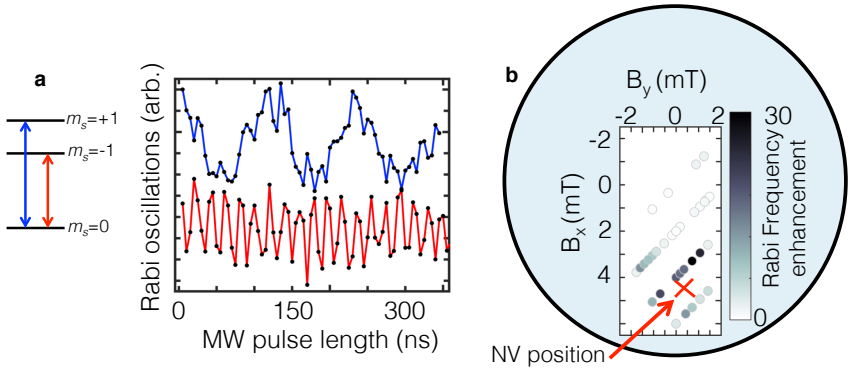

Figure 5. Vortex-induced amplification of spin resonance. (a) Rabi oscillations from $m_s = 0$ to $m_s = +1$ and $m_s = -1$ states of an NV near the vortex core, showing significantly different Rabi frequency. (b) Map of Rabi frequency enhancement as a function of vortex core position. Enhancement is largest when the vortex core approaches the NVs.

from the applied microwave field alone. We conclude that the interaction with the vortex is amplifying the coherent spin rotations. We have mapped out this amplification as a function of vortex core position (Fig. 5b) and find that when the NV-vortex distance is small, we see more than an order of magnitude enhancement. These results suggest that a vortex can be used as an amplifier to increase the sensitivity of NV-based sensors. Another intriguing avenue opened by this effect is to explore spin waves as an intermediary to couple distant NVs.

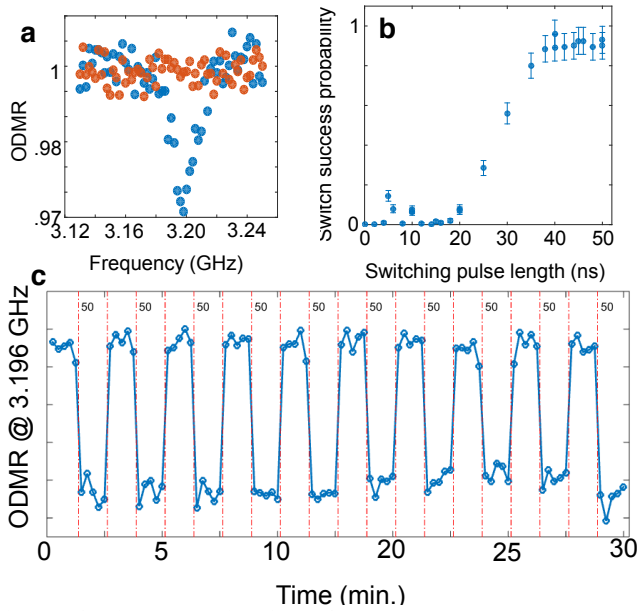

Figure 6. Bistable switching of NV resonances. (a) An NV resonance that is switched on resonance (blue) and off resonance (red) by moving the vortex between bistable positions. (b) Success of NV resonance switching vs. pulse length. (c) Demonstration of reliable, stable switching of an NV resonance over long timescales using single 50 ns pulses.

Mapping the vortex pinning landscape using the technique described above allows us to exploit that effective potential to manipulate the vortex and the NV spins coupled to it [8,9]. In particular, we can find places within the pinning map where two (or more) stable minima exist, providing for fast, low power switching of the vortex core and hence of NV resonances. Switching between one stable point and another can be accomplished with magnetic field pulses of just a few Oersted, with duration ~tens of ns. The displacement of the vortex from one point to the other shifts the NV spin resonances, causing them to switch in and out of resonance with an applied microwave field. Fig. 6a shows two ODMR traces under the same experimental conditions, but with the vortex residing at two different stable points. At one point, a dip indicates the presence of a spin resonance, which is not present at the other point. The switching

between these points can be carried out with a pulse of several Oersted – Fig. 6b shows the switching success vs. pulse time, with reliable switching requiring pulses with several tens of ns duration. Finally, Fig. 6c shows the long-term stability of this switching with a series of switches carried out with individual 50 ns pulses at each red dashed line.

The vortex switching success probability shown in Fig. 6b shows a gradual rise from 20-40 ns, as well as two small but repeatable peaks at shorter time. To understand this behavior, we have carried out a numerical study of vortex dynamics in a bistable potential, in the presence of thermal noise [10]. We found that the dynamics are well described by a set of nonlinear differential equations that can explain the experimental results. Furthermore, the simulations predict rich behavior depending on the parameters of the pinning potential and the driving pulses. In some cases, the peaks at short pulse times can go all the way up to 100% switching probability, providing a route to faster reliable switching of magnetic vortices, for applications in magnetic logic, memory, or spin qubit addressability and control.

Personnel supported:

1. Michael Wolf	Graduate student	full support
2. Robert Badea	Graduate student	full support
3. Evan Telford	Undergraduate	full support (20 hrs./wk)
4. Drew Blasius	Undergraduate	full support (20 hrs./wk)
5. Theodore Rogozinski	Undergraduate	unpaid (volunteer)
6. Joseph Szabo	Undergraduate	full support (20 hrs./wk)
7. Mariel Tader	Undergraduate	partial support (10 hrs./wk)
8. Elisha Haber	Undergraduate	full support (20 hrs./wk)

Publications acknowledging DOE support:

[1] Wolf, M., and J. Berezovsky. "Homogeneous and inhomogeneous sources of optical transition broadening in room temperature CdSe/ZnS nanocrystal quantum dots." *Applied Physics Letters* 105.14 (2014): 143105. (Published)

[2] Berezovsky, J., A. K. Fumani, and M. Wolf. "Room-temperature initialization, dynamics, and measurement of coherent electron spins in strongly confined quantum dots." *SPIE NanoScience+Engineering*. International Society for Optics and Photonics, 2014. (Published)

[3] ElKabbash, M., E. Miele, A. K. Fumani, M. S. Wolf, A. Bozzola, E. Haber, J. Berezovsky, F. De Angelis, G. Strangi. “Room temperature dynamic control of spontaneous emission rate in a single plasmonic nano-cavity” (Submitted, manuscript attached below)

[4] Badea, R., J. A. Frey, and J. Berezovsky. "Magneto-optical imaging of vortex domain deformation in pinning sites." *Journal of Magnetism and Magnetic Materials* (2015). (Published)

[5] Badea, R., and J. Berezovsky. "Mapping the Landscape of Domain-Wall Pinning in Ferromagnetic Films Using Differential Magneto-Optical Microscopy." *Phys. Rev. Appl.* 5.6 (2016): 064003. (Published).

[6] Wolf, M. S. *et al.* Fast nanoscale addressability of nitrogen-vacancy spins via coupling to a dynamic ferromagnetic vortex. *Nat. Commun.* 7:11584 doi: 10.1038/ncomms11584 (2016). (Published).

[7] Badea, R., Wolf, M. S. & Berezovsky, J. Exploiting bistable pinning of a ferromagnetic vortex for nitrogen-vacancy spin control. *Appl. Phys. Lett.* **109,** 132403 (2016). (Published).

[8] Wolf, M. S., Badea, R., Tader, M. & Berezovsky, J. Strong driving of a single coherent spin by a proximal chiral ferromagnet. *Phys. Rev. B* **96,** (2017). (Published).

[9] Badea, R. & Berezovsky, J. Dynamically controlled energy dissipation for fast magnetic vortex switching. *J. Appl. Phys.* **122,** 93904 (2017). (Published).

[10] Haber, E., Badea R. & Berezovsky, J. Simulating the room-temperature dynamic motion of a ferromagnetic vortex in a bistable potential. *Journal of Magnetism and Magnetic Materials.* (Submitted, manuscript attached below.)

Unexpended funds: $0

Room temperature dynamic control of spontaneous emission rate in a single plasmonic nano-cavity

Mohamed ElKabbash[1], Ermanno Miele[2], Ahmad K. Fumani[1], Michael S. Wolf[1], Angelo Bozzola[2], Elisha Haber[1], Jesse Berezovsky[1], Francesco De Angelis[2], Giuseppe Strangi[1,3].

1. Department of Physics, Case Western Reserve University, 10600 Euclid Avenue, Cleveland, Ohio 44106, USA.

2. Instituto Italiano di Tecnologia, via Morego 30, 16163 Genova, Italy.

3. CNR-NANOTEC Istituto di Nanotecnologia and Department of Physics, University of Calabria, 87036-Rende, Italy.

Spontaneous emission (SE) of an emitter arises due to its interaction with the local electromagnetic environment. Accordingly, changing the environment can modify the emission rate. Dynamic, real time, modification of SE rate would enable applications in unconventional optical communication, control of entanglement and dynamic quantum gate operations [1, 2]. Due to the short lifetime of quantum emitters (~1 ns), changing the SE rate dynamically is challenging as it requires modifying the electromagnetic environment at the sub-nanosecond timescale. Recently, dynamic control of quantum dots' (QDs) SE rate was realized in photonic crystal cavities at cryogenic temperatures [1, 3]. Here, we show that plasmonic nano-cavities (PNCs) allow for dynamic control of SE rate at room temperature using a nanoscale integrated platform. We dynamically control the quality factor of a PNC by compensating its plasmonic losses and observe up to six-fold change in the SE rate of QDs coupled to a single PNC [4]. Our results provide basis for novel optical modulators and opens new avenues for plasmonic cavity quantum electrodynamics.

Spontaneous emission rate of an emitter depends on the emitter's electromagnetic environment. In the Wigner-Weisskopf approximation, the SE rate is directly proportional to the electromagnetic local density of states (LDOS) [5, 6, 7]. The LDOS count the electromagnetic modes per unit frequency and per unit volume available for an emitter to radiate into [6, 7]. Accordingly, the LDOS can be modified by placing an emitter inside a cavity; this is the Purcell effect [8].The ratio between the modified and free space emission rates is given by the Purcell factor $F_p \propto Q/V$ where Q and V are the cavity's quality factor and modal volume respectively. Metallic nanostructures with surface features smaller than the incident wavelength support discrete charge density oscillations called localized surface plasmons (LSPs). At resonance, LSPs provide subwavelength light confinement which is useful in many applications[9, 10] such as photovoltaics[11], sensing [12], cancer imaging and photothermal therapy[13] and directional light emission[5, 14]. Because metallic nanostructures can support discrete plasmon modes that form standing waves defined by the geometry of the plasmonic nanostructure[15] they can be described as leaky cavities[16]. The leaky nature of such cavity is because LSPs can decay with the emission of light. Controlling the LDOS in PNCs is the cornerstone of plasmonic cavity quantum electrodynamics (PCQED) [16, 17]. The strong spatial field confinement of plasmonic nano-cavities (PNCs) decreases the cavity effective modal volume and increases the LDOS. Although the Q-factor of PNCs is considerably lower than that of photonic crystal cavities (PCCs) due to strong optical losses in plasmonic nanostructures[18], extreme SE rate enhancement of emitters coupled to PNCs was recently demonstrated in several works[5,19,20,21,22].

In order to dynamically modulate the SE rate of an emitter, the LDOS modulation should take place within timescales shorter than the emitter lifetime. Consequently, dynamic modulation of the SE rate of solid state emitters and fluorescent molecules presents a major challenge due to

their short SE lifetime which is in the order of nanoseconds. Recently, real time, sub-nanosecond modulation of the SE rate of quantum emitters embedded in PCCs was demonstrated. Jin *et al*.[1]controlled the lifetime of quantum dots (QDs) placed inside a photonic crystal cavity (target cavity) by controlling the detuning between the target cavity and an adjacent cavity with a different quality factor (*Q*-factor) and modal volume. Minimizing the detuning between the two cavities redistributes the vacuum field seen by the emitter which corresponded to a change in the effective modal volume and Q factor. Pagilano *et al*.[3]controlled the lifetime of a single QD in a photonic crystal cavity by tuning the exciton energy via the quantum confined Stark effect which changes the QD-cavity coupling strength. However, these approaches are technically complex and were performed at cryogenic temperatures. Furthermore, PNCs outperform PCCs in overcoming the diffraction limit and providing a broadband SE rate enhancement which is more suitable for solid state emitters and fluorescent molecules[6]. In this work, we propose and demonstrate room temperature ultrafast modulation of the SE rate of QDs coupled to PNCs. The SE rate control is based on the dynamic modulation of the PNC *Q*-factor via non-radiative exciton-plasmon resonant energy transfer (RET). Our method does not require complicated device fabrication and relies on an ultrafast phenomenon, *i.e.,* RET, that starts taking place at timescales orders of magnitudes shorter than the emitter lifetime [6, 23]. We demonstrate the proposed effect in CdSe/ZnS QDs coupled to a single, out-of-plane PNC. It is important to study SE rate modulation on emitters coupled to single plasmonic structure in order to avoid spatial inhomogeneity that may affect the gain-plasmon interaction as the SE rate can be affected by the gain location within a plasmonic nanostructure exhibiting various spatial modes [24].

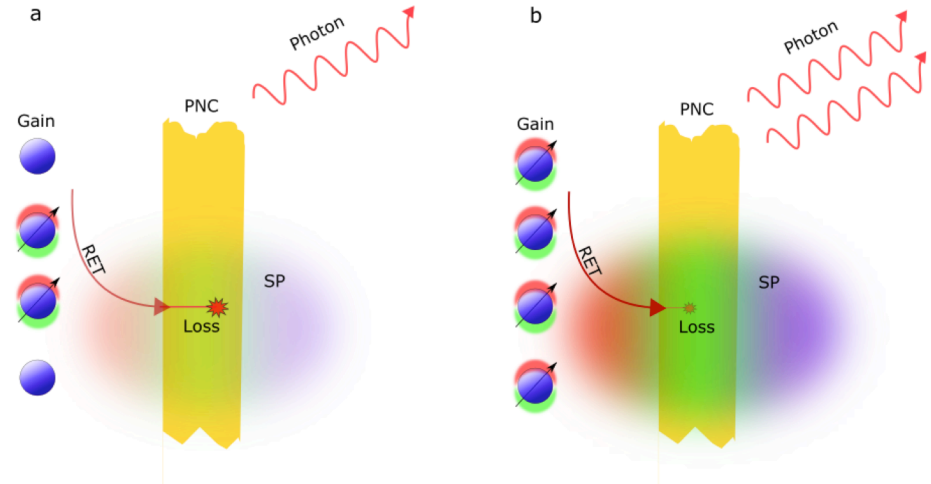

Figure 1|Dynamic SE rate control in PNCs: a, Sketch of the studied system. Some gain is excited and have a finite dipole moment (indicated by an arrow). The excited gain can decay into many channels including transferring its energy to create an SP. The SP can then decay radiatively by creating a photon or non-radiatively due to losses. b, Shows a sketch for the case where more gain is excited. Due to loss compensation, the losses decrease and the cavity *Q*-factor increases. Consequently, the SE rate increases.

Figure 1a illustrates the physical system under consideration. Placing an emitter in close

proximity to a resonant PNC results in non-radiative RET from the emitter to the PNC [6]. The RET condition is satisfied when the emitter emission spectrally overlaps with the PNC surface plasmon resonance [25]. The energy transfer is a dipole-dipole energy transfer, similar to FRET, where the gain decays and creates a surface plasmon, i.e., the gain is weakly coupled to the surface plasmon[6]. The surface plasmon, then, can either decay into a photon or it can be absorbed[6, 18, 26]. In Fig. 1 we are depicting the PNC as a nano-antenna that radiates to the far field at a faster rate than the coupled gain[6, 27, 28]. In addition, gain-plasmon RET is responsible for

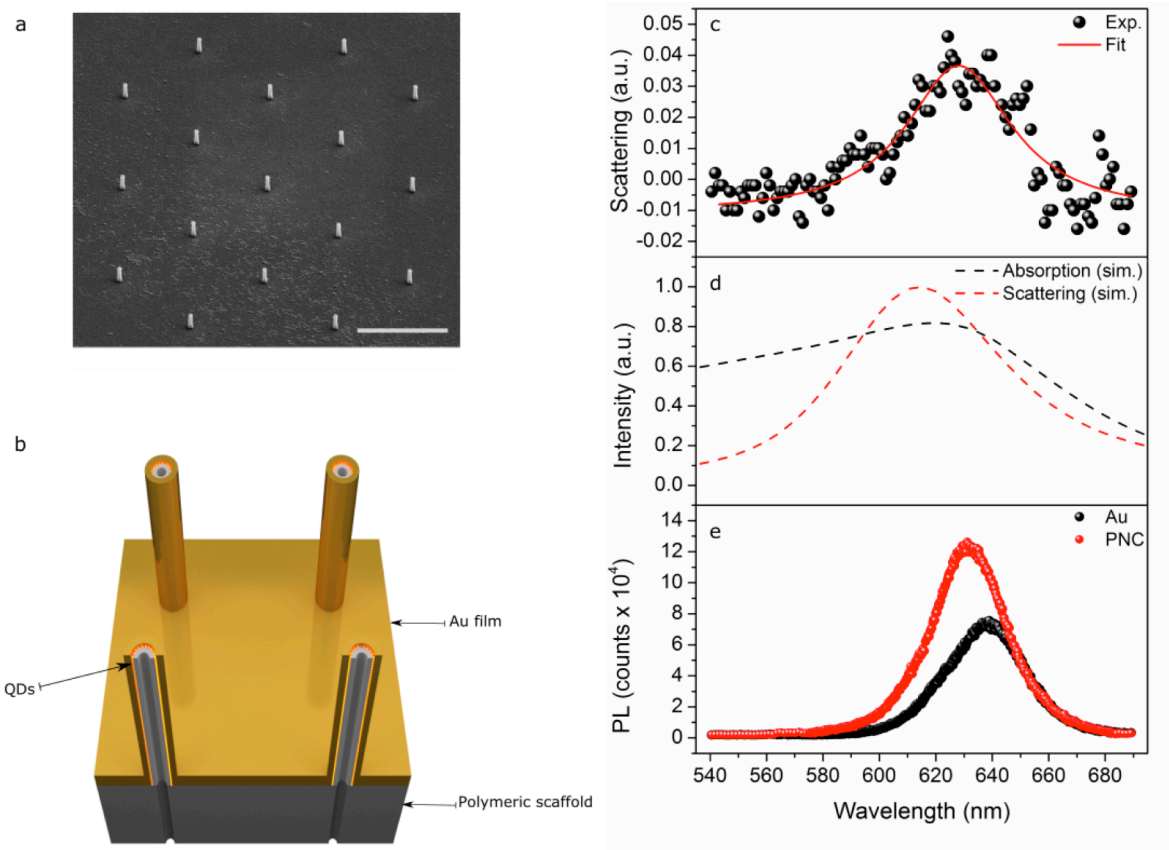

Figure 2| Characterization of integrated plasmonic nano-cavities: a, SEM image of the nano-pillar array (scale bar= 3μm). **b,** a schematic of the nano-pillar PNC, the QDS are spin-coated on a polymeric scaffold, then an Au layer is deposited. **c,** The measured scattering for nano-pillar array; the resonance maximum was determined by fitting the data with a lorentzian function. The measured resonance closely agrees with the simulated absorption (black dashed line) and scattering (red dashed line) presented in **d. e,** Shows the PL of the QD spin coated on an Au film (black spheres) compared to QD incorporated in a single PNC (red spheres)

compensating the plasmonic losses of the PNC [4,18,24, 29,30,31,32,33,34]. Consequently, exciting more gain necessarily means further compensation of PNC plasmonic losses and increasing its Q-factor as shown in Fig. 1b. The increase in the Q-factor leads to our proposed mechanism; increasing the excitation intensity excites more QDs which increases the PNC's Q-factor and subsequently the SE rate [33]. The ratio between the modified SE rates for a given PNC at two different pump powers can be derived directly from the Purcell factor [6, 8] to be $\gamma_1'/\gamma_2' = Q_1/Q_2$ Where $\gamma_1'$and γ_2' are the SE rate for two different pump intensities and Q_1 and Q_2 are the

corresponding PNC *Q*-factors respectively (See *Methods*). Accordingly, by changing the pump intensity, we can dynamically modulate the *Q*-factor of the PNC and modulate the SE rate.

To experimentally verify this approach, we fabricated three dimensional out-of-plane hollow PNCs (Nano-pillars). Figure 2a shows an SEM image of an array of the nano-pillars. The nano-pillars are composed of cylindrical polymeric scaffold, 20 nm thick and 450 nm height, onto which plasmonic shell is formed by coating a 20nm gold layer. The outer and inner diameters of the cavity are approximately 120 and 40 nm, respectively**.** The fabrication procedure is detailed in the methods section. CdSe/ZnS nanocrystal QDs are used as emitters. The QDs are either incorporated by infiltrating them inside the nano-cavities via capillary forces (Supplementary section 1) or by spin-coating the QDs on the polymeric template prior to Au deposition (see Fig. 2b). In order to control for other gain-plasmon interactions that are not related to the modified LDOS via LSP resonance, we prepared a reference sample where the QDs are spin coated on top of an Au film (see *Methods*).

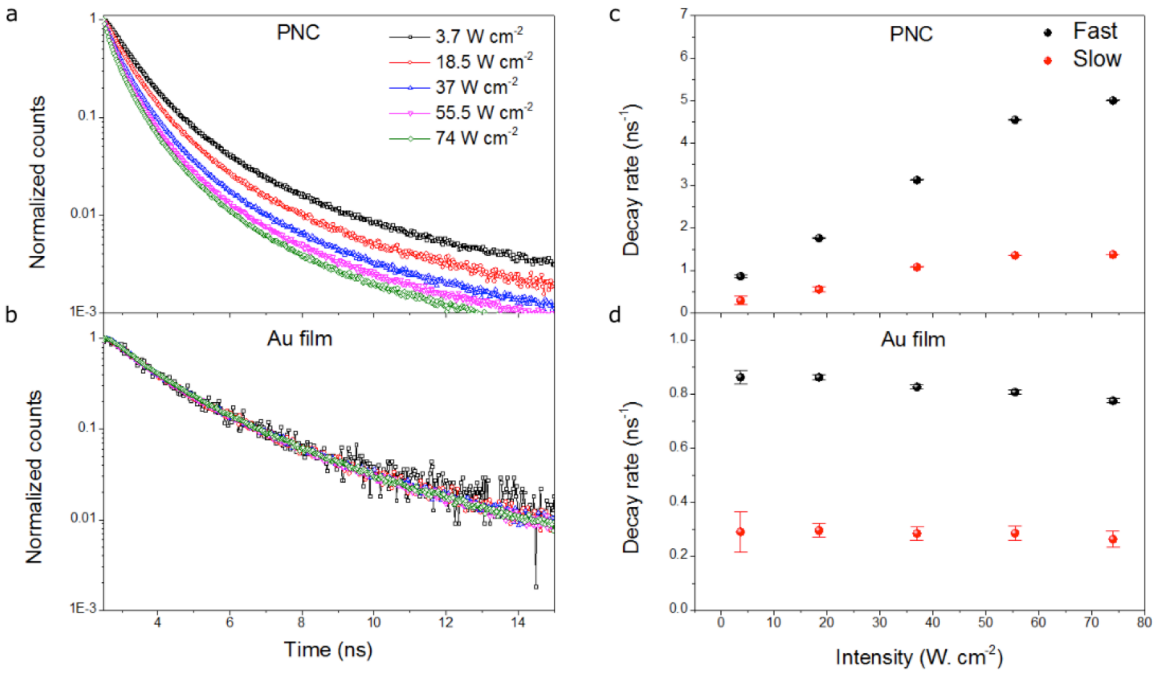

Figure 3| Intensity dependence of SE rate: a, b Measured time-resolved QD emission for five different excitation intensities for the PNC (**a**) and the reference Au film (**b**). The SE lifetime is intensity dependent for the PNC case only. **c,** The fitted SE rate fast component (black spheres) and slow component (red spheres) for the PNC and in **d,** for the reference Au film.

The measured and calculated LSP resonances of the PNC are in close agreement as shown in Fig. 2c and 2d respectively (See *Methods*). In Fig. 2e we compare the QD photoluminescence (PL) collected from a single PNC to PL from the reference sample with excitation pump intensity 18.5 W. cm^{-2}. The excitation wavelength is $490 \pm 20nm$. The PL maximum is blue shifted from 638 nm (reference) to 631nm (PNC) and is pulled towards the LSP resonance peak (~628nm). This is because a PNC changes the spectral shape of emission [35] as it enhances the collected PL near the LSP resonance frequency (Supplementary section 5).

Using a confocal microscope setup (*see Methods)*, we located a single nano-pillar and measured the time-resolved emission of the QDs at emission wavelength 630 nm for a range of pump intensities (3.7 W. cm^{-2}- 74 W. cm^{-2}) and $490 \pm 20nm$ nm excitation wavelength. Figure 3a and

3b show the time-resolved emission collected from a single PNC and the reference Au film respectively. The SE lifetime for the Au film shows no excitation intensity dependence. On the other hand, the SE lifetime from the PNCs strongly depends on the excitation power confirming the validity of our approach. We fitted the time trace of the PL decay with a bi-exponential function and obtained fast and slow SE rate components. By increasing the pump intensity the SE rate increased up to six-fold and fivefold for the fast and slow components respectively. The change in the lifetime as a function of pump intensity is reproducible for all PNCs (Supplementary section 2), however, the extent by which the SE rate changes for a given power range differs from one pillar to another. Such variation is mainly due to variations in the number of spin-coated QDs on different pillars. Since our method relies on the RET from QDs to the PNC, the efficiency of mitigating the PNC losses depends on the number of excited QDs.

To verify the occurrence of loss compensation, we performed confocal pump-probe transient scattering spectroscopy on a single nano-pillar (*see Methods*). It is known that mitigating optical losses of a PNC causes an enhancement in its scattering coefficient[29, 30,31,36,37]. Accordingly, scattering of a probe beam with a wavelength coinciding with the plasmon resonance should increase transiently, if the excited QDs increase the PNC Q-factor. The difference in the probe beam scattering (ΔS) in the case of excited and unexcited QDs is given by $\Delta S = S_{P-R} - S_P - S_R$, where $S_{P\text{-}R}$ is the total collected counts from both the pump and probe pulses irradiating the PNC with a given delay, S_R is the counts from the probe beam only, and S_P is the counts from the pump beam which includes the emission of excited QDs. Since the pump

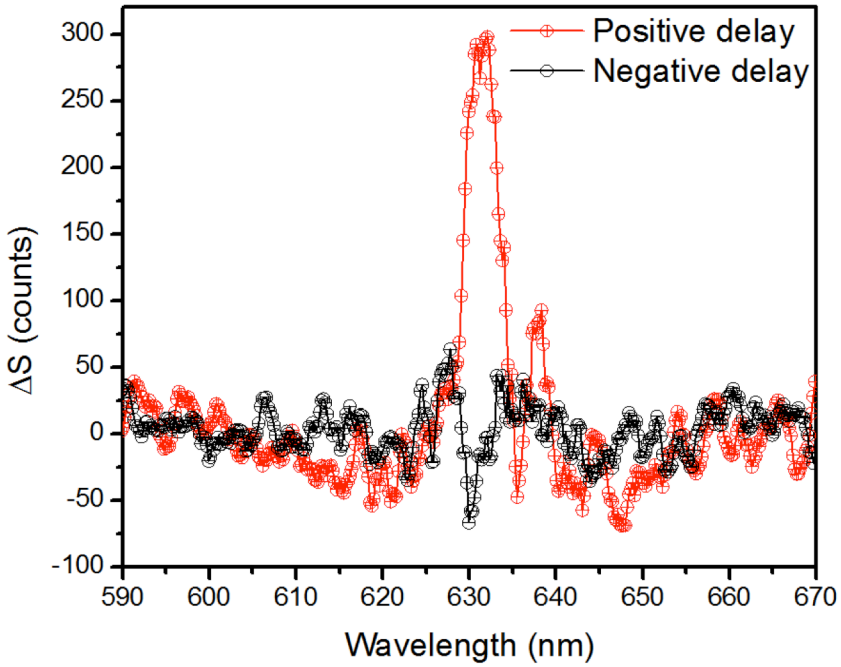

Figure 4| Scattering pump-probe spectroscopy: For positive (black pentagons) and negative (red pentagons) pump-probe delay. The enhanced scattering of the probe beam centered at 630 nm for the positive delay case proves the existence of loss compensation and the gain induced enhancement in the PNC Q-factor.

beam is filtered via a long pass filter (*see Methods)*, we only observe the QD PL for the S_P measurements. One should note that while plasmonic loss mitigation can decrease the transient absorption of the PNC[4], we avoided using transient absorption spectroscopy as it could have led to experimental artifacts related to plasmon resonance bleaching and QDs absorption bleaching [38].

Figure 4 shows the measured ΔS when the probe pulse arrives 0.4 ns after (positive delay) or before (negative delay) the pump pulse. The pump and probe beams are set to $490 \pm 20nm$ and $632 \pm 3nm$ wavelengths respectively. The actual delay between the pump and the probe beams for negative 0.4ns delay is ~ 5 μs (see *Methods*). The stronger scattering of the probe pulse with positive delay indicates an enhanced Q- factor. On the other hand, for the negative delay, the actual delay between the pump and probe is orders of magnitude longer than the QDs lifetime. By the time the probe pulse arrives at the PNC, all QDs had relaxed to the ground state and loss compensation is no longer taking place.

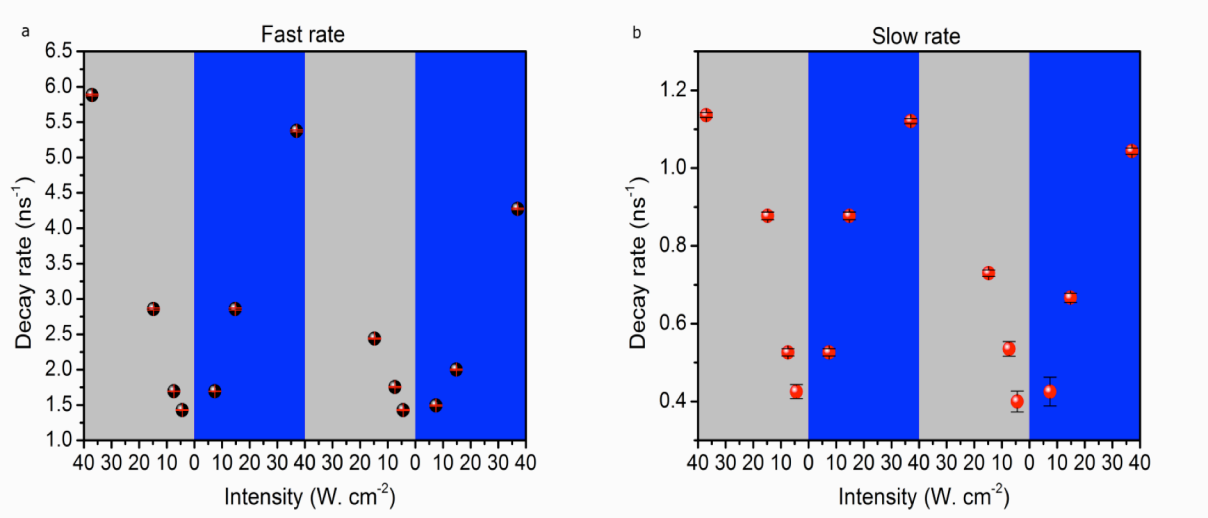

Figure 5|Reversible tuning of SE rate: for **a,** the fast and **b,** slow SE rate components. The excitation intensity is decreasing in the grey shaded region and increasing in the blue shaded region.

In addition to possible PCQED applications, our method can be used for optical modulation. An optical modulator is a device used for manipulating a property of light. In our case, we are interested in the SE rate of an emitter. Figure 5a and 5b show the intensity dependence of the fast and slow components of the SE from a single PNC. The data were collected for four intensities (37, 14.8, 7.4 and 4.4 W. cm^{-2}). The grey shaded regions represent decreasing intensity from 37 to 4.4 W. cm^{-2} while the blue shaded regions represent increasing the intensity from 4.4 to 37 W. cm^{-2}. The ability to reversibly tune the SE rate demonstrates complete control on the SE rate establishing the basis for a novel class of optical modulators. Note that in the fourth region, the SE rates are slightly lower for all pump intensities. This is due to QDs bleaching over long exposure times decreasing the RET efficiency.

Although plasmonic optical losses are considered the major obstacle hindering plasmonics from reaching its full potential[18], we showed that it is possible to convert this weakness into an opportunity. Our approach can be considered a first step towards dissipative driven quantum electrodynamics in PNCs[16, 39]. The simplicity of our approach opens the route for utilizing plasmonics in CQED applications, quantum information and nano-scale optical communication sources. Future works can utilize the ultrafast tunablity of plasmonic optical properties[40, 41] to achieve single photon SE rate modulation for quantum information applications. In addition, any emitter coupled to a PNC should exhibit the SE rate dynamic modulation effect providing it satisfies the RET conditions. Moreover, using emitters that are more stable at higher temperatures is advantageous, e.g., nitrogen vacancies in nano-diamonds and hexagonal boron nitrides[45]. Furthermore, monitoring the change in the SE rate of a stable emitter, it is possible to realize an active plasmon sensor where the change in the SE rate at multiple excitation intensities can be used to reduce the detection sensitivity level. Finally, the ability to dynamically tune the Q-factor of a PNC can be harnessed in other effects where the Q-factor plays an important role, e.g., strong exciton-plasmon coupling. Thus, our approach opens a new avenue for various active plasmonic systems.

Methods

Derivation of the gain permittivity dependence on pump power:

The Q-factor of a PNC embedded in a gain medium is given by[33]

$$Q = \left(\frac{\varepsilon_m''}{\varepsilon_m'} - \frac{\varepsilon_g''}{\varepsilon_g'}\right)^{-1} \frac{\omega\left[\frac{d\,\varepsilon_m'(\omega)}{d\,\omega} + \frac{\varepsilon_m'}{\varepsilon_g'}\frac{d\varepsilon_g'(\omega)}{d\,\omega}\right]}{2\,\varepsilon_m'}$$

where ε_m' and ε_m'' are the real and imaginary permittivity of the metal and ε_g' and ε_g'' are the real and imaginary permittivity of the gain medium and ω is the angular frequency of the incident light. Upon increasing ε_g the plasmonic Q-factor correspondingly increases. The dependence of the gain permittivity on pump power is obtained by following [34]. The gain permittivity for a four-level emitter is given by

$$\varepsilon_g = \varepsilon_0\varepsilon_r + \frac{\sigma_a}{\omega^2 + i\,\Delta\omega_a\omega - \omega_a^2}\,\frac{(\tau_{21}-\tau_{10})\Gamma_{pump}}{1 + (\tau_{32}+\tau_{21}+\tau_{10})\Gamma_{pump}}\,\overline{N_0}$$

Where ε_r is the relative permittivity of dielectric material, τ_{ij} is the decay time for transitioning from state i to the state j. Note that here we are modelling the QD following a four-level rate equation model. If one rewrite this equation taking into account that, $\Gamma_{pump} = \sigma_{abs}\, I_{pump}/\, h\, f_{i\text{-}f}$, where σ_{abs} is the absorption cross section of the emitter and I_{pump} is the pump intensity, and $h\, f_{i\text{-}f}$ is the energy difference between initial and final energy levels we get:

$$\varepsilon_g = \varepsilon_0\varepsilon_r + \frac{\sigma_a}{\omega^2 + i\,\Delta\omega_a\omega - \omega_a^2}\,\frac{(\tau_{21}-\tau_{10})}{\frac{hf_{i-f}}{\sigma_{abs}\,I_{pump}} + (\tau_{32}+\tau_{21}+\tau_{10})}\,\overline{N_0}$$

Accordingly, for higher pump intensity, the gain permittivity increases which in turn increase the quality factor of the PNC.

The Purcell factor is given by $F_p = \frac{\gamma_0'}{\gamma_0} = \frac{3\,Q\,\lambda^3}{4\,\pi^2 V_0}$, where γ_0 and γ_0' are the free space and modified SE rate respectively. Detailed treatment on the effect of PNC on emitters is provided in reference [6]. If the Q factor is modified dynamically, the Purcell factor will modify as well. The ratio between the modified SE rate for different cavity Q factors is thus $\frac{\gamma_1'}{\gamma_2'} = \frac{Q_1}{Q_2}$ where $\gamma_1'$and γ_2' are the SE rate for two different pump intensities and Q_1 and Q_2 are the corresponding PNC Q-factors respectively.

Sample preparations:

Materials:

The quantum dots are Lumidot CdSe/ZnS purchased from Sigma-Aldrich (Quantum Dots, QDs, 640 nm emission peak, core-shell type quantum dots, 5 mg/mL in toluene Sigma-Aldrich,Cat No. 680646-2mL).

Fabrication of plasmonic Nano-pillars:

Out-of-plane plasmonic structures have been fabricated by a focused ion beam assisted nanofabrication technique, described in refs. [42, 43] . We herein slightly modified the fabrication process in order to both incorporate the

emitters in the vertical structures and infiltrate them in the cavity (Supplementary section 1). Shipley S1813 has been deposited by spin coating onto a 100 nm SiNx membrane. Resist thickness has been adjusted to achieve the final 450 nm (±50 nm) nano-pillars height. Polymeric cylindrical scaffold (20 nm wall thickness) is defined by ion milling (Helios Nanolab 620, FEI Co., Hillsboro, OR, USA) to form cylindrical structures. Acceleration voltage was set to be 30 kV with beam current of 40 pA. CdSe/ZnS nanocrystals have been deposited by spin coating (1000 rpm) after dilution to obtain 0.5 mg/mL solution in toluene. Gold (20 nm) was deposited by DC sputter coating in tilted geometry in order to obtain a uniform metal mantel deposited onto gain material. QDs ligands (Hexyldecylamine (HDA), trioctylphosphine (TOPO)) acted as spacer in between gold and CdSe/ZnS. Scanning Electron Microscopy (SEM, Helios Nanolab 620, FEI Co., Hillsboro, OR, USA) was employed to characterize the morphology of fabricated structures. QDs infiltrated structures were prepared by letting diffuse QDs inside nano-pillar cavity. A droplet (10 µl) of 2.5 mg/ml QDs solution was placed on the backside of the membrane of as-milled nano-pillars. Top-side membrane was plased upside-down and put in contact with pure toluene. This configuration by separating QDs-rich toluene solution from the pure toluene solution 11 allowed creating QDs flux and deposition inside nano-cavities. The samples were kept for 5 minutes in saturated toluene atmosphere, and then washed in pure toluene (Sigma-Aldrich Co. LLC, St. Louis, MO, USA). Finally, gold was uniformly deposited onto QDs infiltrated polymeric scaffolds to form 20 nm layer, as previously described. Fabrication of the reference sample: The reference sample is prepared by first depositing a 5 nm Ti adhesion layer on a glass slide, then we deposited 45 nm Au layer. QDs were spin-coated with the same concentration and spin coating parameters used for the QDs spin-coated on the main sample

Fabrication of the reference sample:

The reference sample is prepared by first depositing a 5 nm Ti adhesion layer on a glass slide, then we deposited 45 nm Au layer. QDs were spin-coated with the same concentration and spin coating parameters used for the QDs spin-coated on the main sample.

Simulating the nano-pillars plasmonic resonance:

All the electromagnetic calculations have been carried out using the commercial software Comsol Multiphysics® (RF module). The refractive index of gold was taken from [44] and the values for PMMA from [45]. For the calculations regarding the out-of-plane antennas (Fig. 1d and 1f.), we assumed a TM polarized plane wave with an angle of incidence of 0°. The simulation domain is enclosed within perfectly matched layers (PML) in order to avoid

spurious reflections from the boundaries of the simulation box. The surface is determined by the bottom boundaries of the simulation box and by the metallic bottom-plane.

Experimental setup:

Measuring the LSP resonance of the Nano-pillars:

We used a Leica DM2500P microscope and attached an Ocean Optics HR4000CG optical fiber to turn it to a spectrometer. By placing the sample under a 100X objective lens with NA 0.75, we were able to collect the scattered light through the objective off and on the nano-pillar array. By taking the difference in the scattered light we obtain the distinct scattering of the nano-pillars which corresponds to its plasmon resonance.

Photoluminescence and fluorescence lifetime measurements:

Excitation is provided by a supercontinuum fiber laser (Fianium SC450PP), outputting ≈25 ps duration pulses at a repetition rate of 0.2 MHz. The spectrally broad output of the laser is then filtered by a linearly-graded high-pass and low-pass filter (Edmond optics) mounted on motorized translation stages to tune the cut-on and cut-off wavelengths. The excitation wavelength for the QDs was 490nm with a bandwidth of 20 nm corresponding to its full width half maximum. The excitation (pump) beam is passed through short pass filters with cut-off wavelength of 530 nm. After passing through a 50:50 cube, the beam was then focused on the sample via a 100X objective lens (0.75 NA). The photoluminescence (PL) and scattering is collected again via the 100X microscope objective where we place a long pass 550 nm filter to eliminate the excitation beam when necessary. The PL proceeds to an electron-multiplication CCD (EMCCD) camera/spectrometer to either image the PL or the PL spectrum. By placing the sample on a 3D automated translation stage, we were able to locate the pillars via their PL image. The PL can also be sent to a pair of avalanche photodiodes (APD, PDM-50ct) connected to a time-correlated single photon counting system (TCSPC, Hydraharp 400). The power density was calculated by first measuring the average power before focusing, then determining the beam spot diameter after focusing using the CCD camera. The calculated diameter is ~ 0.6 μm.

Confocal pump-probe setup:

Using the same setup for the PL setup for the excitation pump beam we add a collinear probe beam set at 630nm with FWHM 3 nm. The delay was adjusted manually to be $(\pm 0.4\ ns)$. The repetition rate was 0.2 MHz which

means that the actual delay for -0.4s delay is ~ 5 μs. The delay value was determined using the time-correlated single photon counting system as it can provide the difference in arrival time for the pump and probe with high accuracy. In order to ensure the complete overlap between the pump and probe beams we used the CCD camera configuration in order to see the exact location of the pump beam, probe beam, and photoluminescence from the nano-pillars. We noticed that the QDs emission drops over time when they are exposed to the pump beam which is likely due to photo-thermal plasmonic heating (Supplementary section 3 and 4). Since the magnitudes of SP-R and SP measurements include the QDs emission, which may decrease over time, we performed the SP measurement ex-ante. This measurement order is chosen to avoid any bias in the results towards supporting our claim, i.e., that SP-R magnitude is greater than the sum of SP and SP separately.

Acknowledgments:

The authors would like to thank Eugenio Calandrini for his help in sample preparation. G.S. received funding from the Ohio Third Frontier Project 'Research Cluster on Surfaces in Advanced Materials (RC-SAM) at Case Western Reserve University' and the GU Malignancies Program of the Case Comprehensive Cancer Center. FDA received funding from the European Research Council under the European Union's Seventh Framework Programme (FP/2007-2013)/ERC Grant Agreement no. [616213], CoG: Neuro-Plasmonics. J.B. received support from U.S. Department of Energy, Office of Science, Basic Energy Sciences, under Award #DE-SC008148.

References

1. Jin, C.-Y., Johne, R., Swinkels, M. Y., Hoang, T. B., Midolo, L., van Veldhoven, P. J. , Fiore, A. Ultrafast non-local control of spontaneous emission. *Nat. Nanotechnol*. **9**, 886–890 (2014).
2. S. Kapfinger, T. Reichert, S. Lichtmannecker, K. Müller, J. J. Finley, A. Wixforth, M. Kaniber, H. J. Krenner, Dynamic acousto-optic control of a strongly coupled photonic molecule. *Nat. Commun*. **6**, 8540 (2015)

3. Pagliano, F., Cho, Y., Xia, T., van Otten, F., Johne, R., Fiore, A. Dynamically controlling the emission of single excitons in photonic crystal cavities. *Nat. Commun*. **5**, 5786 (2014).
4. Xiao, S., Drachev, V. P. , Kildishev, A. V. , Ni, X. , Chettiar, U. K.,Yua, H.-K., Shalaev, V. M. Loss-free and active optical negative-index metamaterials. *Nature*, **466**, 735–738 (2010).
5. Akselrod, G. M., Argyropoulos, C., Hoang, T. B., Ciracì, C., Fang, C., Huang, J., Smith, D. R., Mikkelsen, M.H. Probing the mechanisms of large Purcell enhancement in plasmonic nanoantennas. *Nat. Photonics* **8**, 835–840 (2014).
6. Pelton, M. Modified Spontaneous Emission in Nanophotonic Structures. *Nat. Photonics.* **9**, 427−435 (2015).
7. Lodahl, P., Driel, A., Nikolaev, I., Irman, A. Controlling the dynamics of spontaneous emission from quantum dots by photonic crystals. *Nature* **430**, 654–657 (2004).
8. Purcell, E. Spontaneous emission probabilities at radio frequencies. *Phys. Rev*. **69**, 681(1946).
9. Brongersma, M. L., Shalaev, V. M. The case for plasmonics. *Science* **328**, 440–441 (2010).
10. Ozbay, E. Plasmonics: Merging photonics and electronics at nanoscale dimensions. *Science* **311**, 189–193 (2006).
11. Atwater, H. A., Polman A. Plasmonics for improved photovoltaic devices. *Nat. Mat.* **9**, 205–213 (2010).
12. Mayer, K. M. & Hafner, J. H. Localized surface plasmon resonance sensors. *Chem. Rev.* **111**, 3828–3857 (2011).
13. Huang, X., El-Sayed, M. A., Gold Nanoparticles: Optical Properties and Implementations in Cancer Diagnosis and Photothermal therapy. *J. Adv. Res*.**1**, 13−28 (2010).
14. Taminiau, T. H., Stefani, F. D. & van Hulst, N. F. Enhanced directional excitation and emission of single emitters by a nano-optical Yagi–Uda antenna. *Opt. Express* **16**, 10858–10866 (2008).
15. M. Pelton, G. Bryant, G. Introduction to Metal-Nanoparticle Plasmonics. (Wiley, Science Wise Publishing, Hoboken, NJ, USA, 2013).
16. Tame, M. S., *et al.* Quantum plasmonics. *Nature Phys*. **9**, 329–340 (2013).
17. Ginzburg, P. Cavity quantum electrodynamics in application to plasmonics and metamaterials. *Rev. Phys.* **1**, 120– 139 (2016).
18. Khurgin, J. B. How to deal with the loss in plasmonics and metamaterials. *Nature Nanotechnol.* **10**, 2–6 (2015).
19. Russell, K. J., Liu, T., Cui, S. & Hu, E. L. Large spontaneous emission enhancement in plasmonic nanocavities. *Nature Photon.* **6**, 459462 (2012).
20. Kroekenstoel, E. J. A., Verhagen, E., Walters, R. J., Kuipers, L., Polman, A. Enhanced spontaneous emission rate in annular plasmonic nanocavities .*Appl. Phys. Lett.* **95**, 263106 (2009).

21. Kinkhabwala, A. *et al.* Large single-molecule fluorescence enhancements produced by a bowtie nanoantenna, Nat. Photonics **3**, 654-657 (2009).
22. Goffard, J. *et al.* Plasmonic engineering of spontaneous emission from silicon nanocrystals. *Sci. Rep.* **3**, 2672 (2013).
23. Lackowicz, J. R. Principles of Fluorescence Spectroscopy 3rd edn (Springer, 2011)..
24. Hess, O., *et al.* Active nanoplasmonic metamaterials. *Nature Mater*. **11**, 573-584 (2012).
25. El Kabbash M., *et al.* Plasmon-Exciton Resonant Energy Transfer: Across Scales Hybrid Systems. *J Nanomater*, **2016**, 4819040, 21, (2016).
26. Zayats, A. V., Smolyaninov, I. I. & Maradudin, A. A. Nano-optics of surface plasmon polaritons. *Phys. Rep*. **408**, 131–314 (2005).
27. Eggleston M.S., Messer K., Zhan L., Yablonovitch E., Wu,M.C. Optical antenna enhanced spontaneous emission. *Proc. Nat. Acad. Sci*., **112**, 1704–1709 (2015).
28. Krasnok, A. E. et al. An antenna model for the Purcell effect. *Sci. Rep* . **5**, 12956 (2015).
29. Lawandy, N. M. Localized surface plasmon singularities in amplifying media. *Appl. Phys. Lett.* **85**, 5040–5042 (2004).
30. Noginov, M. A., *et al*. Enhancement of surface plasmons in an Ag aggregate by optical gain in a dielectric medium. *Opt. Lett*. **31**, 3022–3024 (2006).
31. Smuk A. Y., Lawandy, N. M.. Spheroidal particle plasmons in amplifying media. *Appl. Phys. B* **84**, 125-129 (2006).
32. M. A. Noginov. Compensation of surface plasmon loss by gain in dielectric medium. *J. Nanophotonics* **2**, 021855–1–17 (2008).
33. Wang, F. , Shen, Y. R. General properties of local plasmons in metal nanostructures. *Phys. Rev. Lett.* **97**, 206806 (2006).
34. Campione, S., Albani, M., Capolino, F., Complex modes and near-zero permittivity in 3D arrays of plasmonic nanoshells: loss compensation using gain [Invited]. *Opt. Mater. Express* **1**, 1077 (2011).
35. Ringler, M., *et al.* Shaping emission spectra of fluorescent molecules with single plasmonic nanoresonators. Phys. Rev. Lett. 100, 203002 (2008).
36. De Luca, A., *et al.* Dispersed and Encapsulated Gain Medium in Plasmonic Nanoparticles: A Multipronged Approach to Mitigate Optical Losses. *ACS Nano*, 5823–5829 (2011).
37. Rashed, A. R., *et al.* Battling Absorptive Losses by Plasmon−Exciton Coupling in Multimeric Nanostructures. *RSC Adv.* **5**, 53245−53254 (2015).
38. ElKabbash, M., *et al.* Ultrafast transient optical loss dynamics in exciton–plasmon nano-assemblies, *Nanoscale*, **9**, 6558-6566 (2017) .
39. Verstraete, F., Wolf, M. M. & Cirac, J. I. Quantum computation and quantum-state engineering driven by dissipation. *Nature Phys.* **5**, 633636 (2009).
40. Guo, P., Schaller, R. D., Ketterson, J. B., Chang, R. P. H. Ultrafast switching of tunable infrared plasmons in indium tin oxide nanorod arrays with large absolute amplitude. *Nat. Photonics*. **10**, 267–273 (2016).

41. Yang,Y., Kelley, K., Sachet, E., Campione, S., S. Luk, T., Maria, J.,-P., Sinclair, M. B., Brener, I. Femtosecond optical polarization switching using a cadmium oxide-based perfect absorber . *Nat. Photonics.* **11**, 390–395 (2017).
42. Malerba, M. et al. 3D vertical nanostructures for enhanced infrared plasmonics. *Sci*. *Rep*. **5**, 16436 (2015).
43. De Angelis, F. et al. 3D hollow nanostructures as building blocks for multifunctional plasmonics. *Nano Lett*. **13**, 3553–3558 (2013).
44. Ma, R.-M., Ota, S., Li, Y., Yang, S. & Zhang, X. Explosives detection in a lasing plasmon nanocavity. *Nat. Nanotechnol*. **9**, 600–604 (2014).
45. Tran,T. T., Bray, K., Ford, M. J., Toth, M., Aharonovich, I. Quantum emission from hexagonal boron nitride monolayers, *Nat. Nanotechnol*. **11**, 37–41 (2016).

Simulating the room-temperature dynamic motion of a ferromagnetic vortex in a bistable potential

E. Haber[a], R. Badea[a], J. Berezovsky[a,*]

[a]*Department of Physics, Case Western Reserve University, Cleveland, Ohio 44106, USA.*

Abstract

The ability to precisely and reliably control the dynamics of ferromagnetic (FM) vortices could lead to novel nonvolatile memory devices and logic gates. Intrinsic and fabricated defects in the FM material can pin vortices and complicate the dynamics. Here, we simulated switching a vortex between bistable pinning sites using magnetic field pulses. The dynamic motion was modeled with the Thiele equation for a massless, rigid vortex subject to room-temperature thermal noise. The dynamics were explored both when the system was at zero temperature and at room-temperature. The probability of switching for different pulses was calculated, and the major features are explained using the basins of attraction map of the two pinning sites.

Keywords: magnetic vortex, magnetization switching, thermal noise

1. Introduction

Precise control over the dynamic motion of ferromagnetic (FM) vortices could be used to create new spin-based memory and quantum computing devices. Quickly and reliably moving a vortex domain wall out of one pinning site and into another (switching) in magnetic nanowires has been proposed as a method to build faster non-volatile magnetic memory devices. [1] Similarly, switching between two bistable pinning sites can be used for logic operations. [2] Nitrogen-vacancy spins have been used to create potentially scalable room-temperature quantum registers, [3] and vortices provide a strong, localized magnetic field gradient capable of addressing and controlling the individual spins. [4, 5] Furthermore, much recent attention has focused on vortex-like topologically stabilized spin textures (e.g. skyrmions) [6], which likely will display qualitatively similar dynamics to the vortices studied here. In all of these devices, pinning sites that are intrinsic to the fabrication process can impact the dynamics, and this effect must be understood in order to reliably control the vortex motion.

*Corresponding author

Email address: jab298@case.edu (J. Berezovsky)

The ground state magnetization distribution of a thin micron-scale FM disk is a vortex state. [7, 8] The magnetization is in-plane, circularly symmetric, and tangential to the disk boundary everywhere except at the disk center, where it is out-of-plane and parallel to the rotation axis of the disk. The core region of the vortex has a half width ~ 10 nm, which is set by the exchange length. [9] In the rigid vortex model, changes to the magnetization distribution outside the core are ignored as the vortex is moved around the disk. [10] This simplifying assumption allows the displacement of the vortex core from the center of the disk to be specified using a single parameter $\mathbf{x} = (x, y)$.

The motion of the vortex can be controlled with magnetic fields. Applying an in-plane field shifts the equilibrium position of the vortex. When the vortex is excited, the core will enter a circular, damped precession around its equilibrium position at a characteristic frequency. [11] The value of this gyrotropic frequency is dependent on both the geometry of the disk, as well as the gradient of the local pinning potential. [12]

For disks with intrinsic or fabricated defects, it has been shown that the vortex core can become pinned if the widths of the defects are comparable to that of the vortex core because they lower the vortex's energy. [13, 14, 15] By measuring either the hysteretic displacement of the vortex as it is slowly moved across the disk, [14, 15, 5] or its gyrotropic frequency for small excitations when it is trapped in a pinning site, [16] the local pinning potential can be mapped out. Past research has found that approximating the pinning sites as symmetric Gaussian wells adequately reproduces measured hysteresis in the pinning potential. [14, 15, 5]

Previously, an experiment was performed to study vortex switching in a bistable potential. [5] The vortex was initialized in one of the pinning sites, a magnetic field pulse was used to free it from the initialization site, and the probability, P, of it ending up in the target site was measured versus the magnetic field pulse duration, τ. It was found that $P \approx 0$ for short τ, there was a gradual rise centered around $\tau \approx 27$ ns, and by $\tau \approx 50$ ns it had saturated at $P \approx 80\%$. This timescale for saturation was attributed to the vortex settling into the target site because the expected vortex relaxation time was ~ 50 ns. It was also observed that there were small bumps in P close to multiples of the gyrotropic period. Here we look to use a simple model for the vortex dynamics in a bistable pinning potential under the influence of thermal noise to reveal the mechanisms behind these features.

The gyrotropic response of the vortex on an ideal disk (no pinning) under the influence of thermal noise has been previously studied, [17, 18, 19, 20] and we seek to use a similar stochastic model to simulate the gyrotropic response to a field pulse in a bistable potential. Experimental data [5] is currently limited to a highly asymmetric potential where the target site is significantly weaker than the initialization site. In addition to studying this pinning configuration, we explored how the switching behavior depends on the relative stability of these two sites.

2. Model of the system

The dynamics of the vortex during the switching process is modeled by assuming that the vortex is rigid, massless, and that the dominant source of noise is thermal. Using the rigid vortex model, and approximating the restoring force as linear and the pinning sites as symmetric Gaussian wells, the potential seen by the vortex can be written as

$$U = \frac{1}{2}k|\mathbf{x}|^2 - ck\chi_0(B_y x - B_x y) - \sum_{n=1}^{N} d_n e^{-\frac{|\mathbf{x}-\mathbf{x}_n|^2}{2w_n^2}}, \tag{1}$$

where k is the stiffness coefficient, $c = \pm 1$ is the vortex chirality (the magnetization around the vortex core is either clockwise or counter-clockwise), χ_0 is the displacement susceptibility, $\mathbf{B} = (B_x, B_y)$ is the in-plane applied magnetic field, d_n is the depth of the n^{th} pinning site, $\mathbf{x}_n$ is the position of the n^{th} pinning site, w_n is the width of the n^{th} pinning site, and N is the total number of pinning sites.

The first two terms in Eq. 1 model an ideal disk where U is a smooth paraboloid with only one equilibrium point (ideal potential). For $|\mathbf{B}| \neq 0$ this global minimum is linearly displaced from the center of the disk $\mathbf{x} = (0, 0)$, to $\mathbf{x} = c\chi_0(B_y, -B_x) \equiv (\beta_y, -\beta_x)$ where $\chi_0 = 90$ nm/mT in this case. In the simulations, β_x was always set to 0, and the amplitude of the magnetic field is given by $\beta_y = \beta$ in units of distance. A nonzero β causes the global minimum of the ideal potential to shift linearly, thus its location is given by $\mathbf{x} = (\beta, 0)$. In this paper, a potential with two bistable pinning sites is studied (in Eq. 1, $N = 2$). $d_n = 20$ eV, $w_n \approx 25$ nm, $\mathbf{x}_1 = (65 \text{ nm}, 0)$, and $\mathbf{x}_2 = (-65 \text{ nm}, 0)$ were chosen because they are similar to pinning sites that have been examined experimentally. [5]

When $\beta = 0$ the two pinning sites have equivalent strengths, and the potential is symmetric. $U(x)$ along the line $y = 0$ is plotted in red in Fig. 1(a), which shows that the two pinning sites are equally deep, wide, and equidistant from $x = 0$. If $\beta < 0$ then the potential becomes tilted towards the initialization site, causing it to become stronger than the target site. The blue curve in Fig. 1(a) corresponds to $\beta = -30.5$ nm, and it can be seen that the initialization site has become deeper and wider than the target.

Hysteretic displacement of the vortex core equilibrium position for this pinning potential was observed by initializing the vortex core at $\mathbf{x} = (\pm 200 \text{ nm}, 0)$, sweeping β down or up, and at each value of β measuring the equilibrium position of the vortex, $x_{eq}(\beta)$ (Fig. 1(a) inset). The green curve shows $x_{eq}(\beta)$ when the field is swept up, and the purple curve $x_{eq}(\beta)$ when it is swept down. Hysteresis can be seen as there are several ranges of β for which the local minimum of U that the vortex settles into is different depending on the sweep direction. These regions of β for which there are multiple x_{eq} indicate bistability.

The possible amplitudes and offsets for magnetic field pulses that can be used to study bistable switching can be extracted from the hysteretic displacement curve. It can be seen in the inset of Fig. 1 (a) that there is a relatively large

region of bistability from $\beta = -40 \rightarrow 40$ nm. Choosing the initial value of β to be in this region and then pulsing out of it frees the vortex to precess around a single equilibrium position as one of the pinning sites is now unstable.

A magnetic field pulse profile used for switching is illustrated in the inset to Fig. 1(b). The amplitude of the magnetic field is denoted by $\beta = \beta_0$ when the pulse is turned off, where β_0 lies in the region of bistability. The field is given by $\beta = \beta_p$ when the pulse is on, where β_p lies outside the bistable region. U for $\beta = \beta_0$ (solid line) and $\beta = \beta_p$ (dashed line) is shown in Fig. 1(b) for the pulse profile shown in the inset. It can be observed that U is just barely bistable when $\beta = \beta_0$, and when $\beta = \beta_p$ only the target site is stable with the initialization site now slightly unstable.

β rises from β_0 to β_p with a total rise time $t_r = 2$ ns, it remains on for some length of time $\tau - 2t_r$, and finally returns to β_0. t_r was chosen so that the displacement of the vortex in time during the switching process would be similar to experimental obervations. In these simulations, $\beta_0 = 0$ was used for a symmetric potential, $\beta_0 = -30.5$ nm was used as the offset for an asymmetric potential, and $\beta_p = 42$ or 51 nm were used for the pulse field, unless otherwise specified.

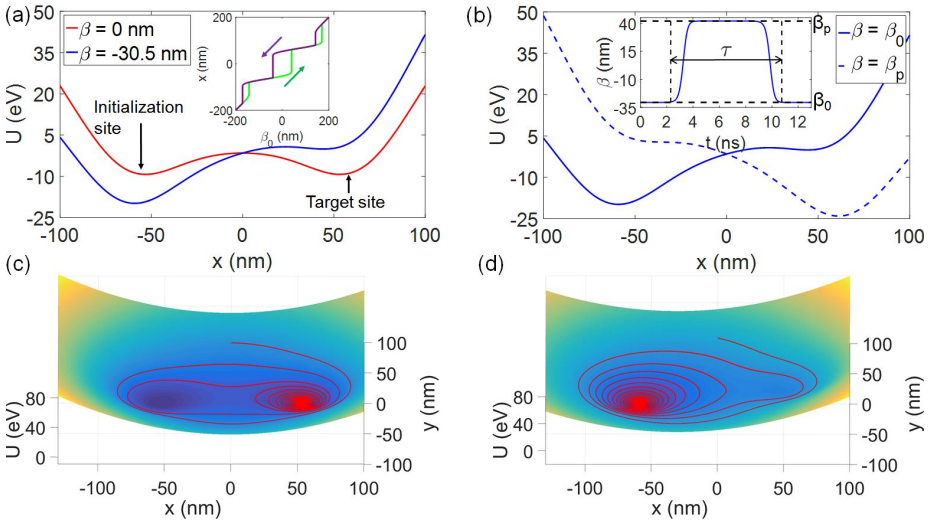

Figure 1: Pinning potentials. (a) $U(x)$ along $y = 0$ where the red curve corresponds to the symmetric potential $\beta_0 = 0$, and the blue curve to the asymmetric potential $\beta_0 = -30.5$ nm. The inset shows the equilibrium position of the vortex x_{eq}, versus β_0 when the vortex is started to the left of both pinning sites and β_0 is swept up (green), and to the right of both and β_0 is swept down (purple). (b) $U(x)$ along $y = 0$ for $\beta_0 = -30.5$ nm before the pulse (blue) and during the pulse (dashed blue), for $\beta_p = 42$ nm. The inset displays a pulse used in the switching measurement. Initially, $\beta = \beta_0$, then it rises to $\beta = \beta_p$ in time t_r, it remains at β_p for a length of time $\tau - 2t_r$ before falling back to β_0. (c) and (d) 3D colormap plots of $U(x, y)$ calculated from Eq. 1 for $\beta_0 = 0$ and $\beta_0 = -30.5$ nm respectively. The red paths show $\mathbf{x}(t)$ calculated from Eq. 2 for the corresponding β_0 where the vortex was started from $\mathbf{x}_0 = (0, 70\text{nm})$.

The vortex dynamics in a potential given by Eq. 1 can be obtained from the Landau-Lifshitz equation, [21, 22, 20] and for disks with thicknesses $\lessapprox 50$ nm and micron-scale diameters, the intrinsic vortex mass is negligible. [23, 24, 25, 26] Also, assuming that the vortex is rigid, its trajectory is given by the Thiele equation

$$-\mathbf{G}\times\dot{\mathbf{x}}-\alpha\dot{\mathbf{x}}+\nabla U+\mathbf{F}_s=\mathbf{0}, \tag{2}$$

where α is a damping factor, $\mathbf{G}=-2\pi LM_s\mu_0 p\hat{\mathbf{z}}/\gamma$ is the gyrotropic vector of a disk with a thickness L, saturation magnetization M_s, and gyromagnetic ratio γ, $p=\pm 1$ is the vortex polarity (magnetization at the core is either parallel or anti-parallel to the unit vector $\hat{\mathbf{z}}$), μ_0 is the vacuum permeability, and $\mathbf{F}_s$ is a stochastic force term that accounts for thermal noise.

The first term in Eq. 2 is the gyroforce, which points in-plane perpendicular to the vortex's velocity, and results in circular motion about the equilibrium point. The second term accounts for damping, which causes the vortex to lose energy while it precesses. The third term is the force due to U, and the last term accounts for thermal noise and is given by the fluctuation-dissipation theorem

$$\langle F_{s,i}(t)\rangle=0, \tag{3}$$

$$\langle F_{s,i}(t)F_{s,j}(t')\rangle=2\alpha k_BT\delta(t-t')\delta_{ij}, \tag{4}$$

where i and j are either of the in-plane Cartesian coordinates, t and t' are any two times, k_B is the Boltzmann constant, T is the temperature of the system, δ is the Dirac delta function, and δ_{ij} is the Kronecker delta. Room-temperature noise is assumed, and in these simulations β_p is large enough that the vortex's gyrotropic response dominates over the thermally driven random motion.

Fig. 1(c) shows a 3D colormap plot of $U(x,y)$ calculated from Eq. 1 for $\beta_0=0$. The red curve corresponds to $\mathbf{x}(t)$ calculated from Eq. 2 for $T=0$ (so the equation is deterministic). The vortex was started at $\mathbf{x}_0=(0,70\text{nm})$, and allowed to freely precess until it landed in the target site. Fig. 1(d) shows a 3D colormap of $U(x,y)$ for $\beta_0=-30.5$ nm, along with $\mathbf{x}(t)$ for $T=0$ in red. The vortex was again started from $\mathbf{x}_0=(0,70\text{nm})$, but in the asymmetric potential it fell into the initialization site. It can be seen that the two $\mathbf{x}(t)$ are similar, but for $\beta_0=-30.5$ nm the initialization site is large enough to trap the vortex during its second precession, whereas in the symmetric case the vortex had enough energy to make it over the barrier and land in the target site during the second precession.

In the simulations we used parameters for thin Permalloy disks with 2 μm diameters and $L=40$ nm. We set $M_s=0.8$ A/μm, $k=2\pi f_g|\mathbf{G}|$ where the gyrotropic frequency is $f_g=136$ MHz, and $\gamma=2.2\times10^5$ m/A·s. $\alpha=0.03|\mathbf{G}|$ was selected to be similar to experimentally observed values.

3. Dynamics at zero temperature

The goal of the simulations was to understand the vortex motion when attempting to switch it from one pinning site to another, and how these dynamics

determine the probability of switching P for different pulse lengths τ. We first examine the simpler case in the absence of thermal noise. Eq. 2 was solved for a potential given by Eq. 1 when $T = 0$ K, and thus $\mathbf{F}_s = \mathbf{0}$, using the MATLAB ODE solver. To simulate the switching process, the vortex was started in the initialization pinning site ($\beta = \beta_0$), a magnetic field pulse was used to tilt the potential ($\beta = \beta_p$), see Fig. 1(b), and knock the vortex out of the initialization site so that it precessed around the target site for some time τ. Once the pulse ended ($\beta = \beta_0$) the vortex would eventually fall into one of the two bistable pinning sites, as shown in Fig. 1(c) and 1(d). A successful switch was defined as the vortex settling into the target site after the pulse ends.

We denote the deterministic ($T = 0$ K) trajectory of the vortex over time t, for a given τ as $\mathbf{x}_d(t;\tau)$. The position of the vortex when the pulse turns off, $\mathbf{x}_d(\tau;\tau)$, completely determines which pinning site the vortex will eventually fall into because, for $T = 0$ K, Eq. 2 is deterministic, and the vortex has no momentum. Regardless of what pulse amplitude and length were used to put the vortex in some location $\mathbf{x}_d(\tau;\tau)$, or if it was started there, it will always follow the same path from that point in time since $\dot{\mathbf{x}}$ is determined solely by $\mathbf{x}$ for a given U. By mapping out which starting positions, $\mathbf{x}_0$, result in the vortex falling into which pinning sites the behavior of $P(\tau)$ can be understood.

If, for a given $\mathbf{x}_0$, the vortex landed in the initialization site then that point was added to the set of points, B_i, that feed into the initialization site. If instead the vortex would eventually settle into the target site, then that $\mathbf{x}_0$ was added to the set of points, B_t, that result in the vortex falling into the target site. The sets of initial points B_i and B_t are the basins of attraction of the initialization and target sites, respectively. The basins of attraction for $\beta_0 = 0$ and $\beta_0 = -30.5$ nm are shown in Fig. 2(a) and 2(b). Points that are in B_i are colored white, while those that are in B_t are colored gray. To construct each basins of attraction map, the magnetic field was set to a constant value $\beta = \beta_0$, the vortex was initialized at different positions in the pinning potential, $\mathbf{x}_0$, and then it was allowed to freely precess into one of the two pinning sites.

It can be seen that each basin has a spiral shape. Each pinning site (centered on $\mathbf{x} = (\pm 65\text{nm}, 0)$) lies in a region where the corresponding basin of attraction is relatively wide. Farther out along the spiral both basins become narrower at first, and then slowly wider as they continue to spiral away from the pinning sites. The basins for the asymmetric potential, shown in Fig. 2(b), are similar to the symmetric basins except that the disparity in strength between the two pinning sites results in the target basin being significantly more narrow at each point on the spiral when $\beta_0 = -30.5$ nm than when $\beta_0 = 0$.

The behavior of $P(\tau)$ for $T = 0$ K and any pulse amplitude can be read off of the basins of attraction map and the corresponding $\mathbf{x}_d(\tau;\tau)$, which, for $\beta_p = 42$ nm, is shown by the black curve in Fig. 2(a) and (b). When the vortex is not subject to thermal fluctuations, and is massless, it must stay in whichever basin it was in when the pulse finished turning off. Since there is no uncertainty for $T = 0$ K, $P(\tau)$ can only be one of two values:

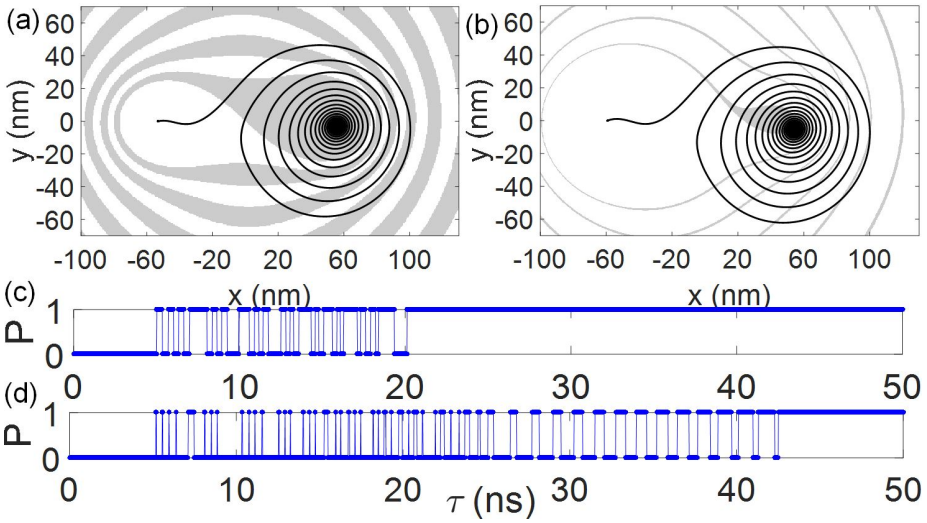

Figure 2: Basins of attraction and switching for $T = 0$ K. (a) the basins of attraction for $\beta_0 = 0$. Starting positions were colored gray if the vortex landed in the target site, and white if it settled into the initialization site. The black curve is $\mathbf{x}_d(\tau;\tau)$ where τ was swept from 0 to 50 ns in steps, and $\beta_p = 42$ nm. (b) the two basins of attraction for $\beta_0 = -30.5$ nm. (c) and (d) $P(\tau)$ for $\beta_0 = 0$ and $\beta_0 = -30.5$ nm respectively, where τ was again swept from 0 to 50 ns, and $\beta_p = 42$ nm.

$$P(\tau) = \begin{cases} 0, \mathbf{x}_d(\tau;\tau) \in B_i \\ 1, \mathbf{x}_d(\tau;\tau) \in B_t \end{cases}$$

$P(\tau)$ for $\beta_0 = 0$, $\beta_p = 42$ nm, and $T = 0$ K is given in Fig. 2(c). This plot can be viewed as an "unwrapped" version of the black spiral in Fig. 2(a), where $P(\tau) = 0$ ($P(\tau) = 1$) when the black spiral crosses a white (gray) region. For $\tau < 5$ ns, $P(\tau) = 0$, which shows that for these short τ the vortex is unable to make it into the target's basin of attraction, B_t. For $5 \lessapprox \tau \lessapprox 7.5$ ns fast oscillations in $P(\tau)$ occur approximately every 0.2 ns. These are due to $\mathbf{x}_d(\tau;\tau)$ cutting through the basins of attraction on this timescale. At $\tau \approx 7.5$ ns there is a wide peak where $P(\tau) = 1$. This occurs near the half-period of the precession because $\mathbf{x}_d(\tau;\tau)$ can be seen to run along the target's basin for a relatively large range of τ. For $7.5 \lessapprox \tau \lessapprox 10$ ns fast, 0.2 ns oscillations can again be seen due to the vortex quickly cutting in and out of the basins once more. For $10 \lessapprox \tau \lessapprox 11$ ns a relatively wide trough followed by a relatively wide peak in $P(\tau)$ can be observed. In Fig. 2(a), near the first period of the vortex's precession, $\mathbf{x}_d(\tau;\tau)$ initially runs through a wide section of B_i immediately followed by a wide section of B_t. Both basins are wide here because near the period of the vortex's precession it runs in between the two pinning sites, resulting in a wide trough followed by a wide peak in $P(\tau)$.

For longer τ the pattern in $P(\tau)$ is similar. In between the half-period and

period of the vortex's precession fast ~ 0.2 ns oscillations in $P(\tau)$ can be seen. Near the half-period of precession the vortex will often run along one of the two basins, resulting in either a single peak or trough in $P(\tau)$. For τ close to the period of precession there is a relatively wide trough followed immediately by a peak. As the vortex settles into the target site for longer τ, however, the period of the precession becomes shorter due to the increased steepness of the potential in the pinning sites. In $P(\tau)$, this results in a shorter separation in time between relatively wide peaks and troughs. Additionally, $\mathbf{x}_d(\tau;\tau)$ spends more time in B_t as the vortex falls into the target site, since B_t becomes larger closer to the target. This leads to more $P(\tau) = 1$ as τ approaches 20 ns. For $\tau > 20$ ns all $P(\tau) = 1$, which can be seen in Fig. 2(a) as being due to all $\mathbf{x}_d(\tau;\tau)$ lying in B_t as the vortex settles into the target site while the pulse is still on.

$P(\tau)$ for $\beta_0 = -30.5$ nm is plotted in Fig. 2(d) and has similar features to $P(\tau)$ for $\beta_0 = 0$. In between the half-period and period of precession $\mathbf{x}_d(\tau;\tau)$ lies primarily in the initialization site's basin except when it briefly cuts across B_t. Due to the reduced width of the target basin it only takes ~ 0.1 ns for the vortex to pass through each segment of B_t. Near the half-period of the vortex's precession it is again possible for $\mathbf{x}_d(\tau;\tau)$ to run along B_t, resulting in peaks in $P(\tau)$ that exceed 0.1 ns in width. For $\tau \gtrapprox 25$ ns wide troughs followed by increasingly wide peaks become visible in $P(\tau)$. These correspond to the period of the vortex's precession and are due to $\mathbf{x}_d(\tau;\tau)$ running close to the target site so that the target's basin is wide enough for the peaks in $P(\tau)$ to be significantly larger than 0.1 ns. For $\tau > 43$ ns, all $P(\tau) = 1$ because the vortex has been given enough time to settle into the target site during the pulse.

By sweeping both β_p and τ, the entire phase-space of $P(\beta_p, \tau)$ can be mapped out both for $\beta_0 = 0$ (Fig. 3(a)) and $\beta_0 = -30.5$ nm (Fig. 3(b)), quantifying the general trends illustrated by the basins of attraction maps in Fig. 2. If a combination of β_p and τ resulted in a successful switch ($P(\beta_p, \tau) = 1$) then that point was colored gray, if instead $P(\beta_p, \tau) = 0$ then the point was colored white. The horizontal line $P(\beta_p = 42\text{nm}, \tau)$ in Fig. 3(a) is identical to $P(\tau)$ in Fig. 2(c), as with $P(\beta_p = 42\text{nm}, \tau)$ in Fig. 3(b) and $P(\tau)$ in Fig. 2(d). The different regions of Fig. 3 show all of the possible dynamics in P that result from different pulses.

The purely white region A in Fig. 3 is comprised of pulses that are too short or too weak to break the vortex free from the initialization site. The wide features of region B are due to the vortex running along either the target or initialization site's basin at odd integer multiples of the half-period. The relatively wide vertical stripes in region C shows that at integer multiples of the gyrotropic period the vortex first passes through a broad region of B_i followed immediately by a broad region of B_t. The sharp features of region D indicate that in between half-periods the vortex quickly cuts into and out of different basins, resulting in sharp vertical lines. The large, gray region E corresponds to values of β_p for which the equilibrium position when the pulse is on lies inside the target site. Thus, for τ long enough that the vortex has time to settle into the target site, when the pulse turns off the vortex will remain trapped in the target site. For β_p and τ slightly to the left of region E, the features that occur

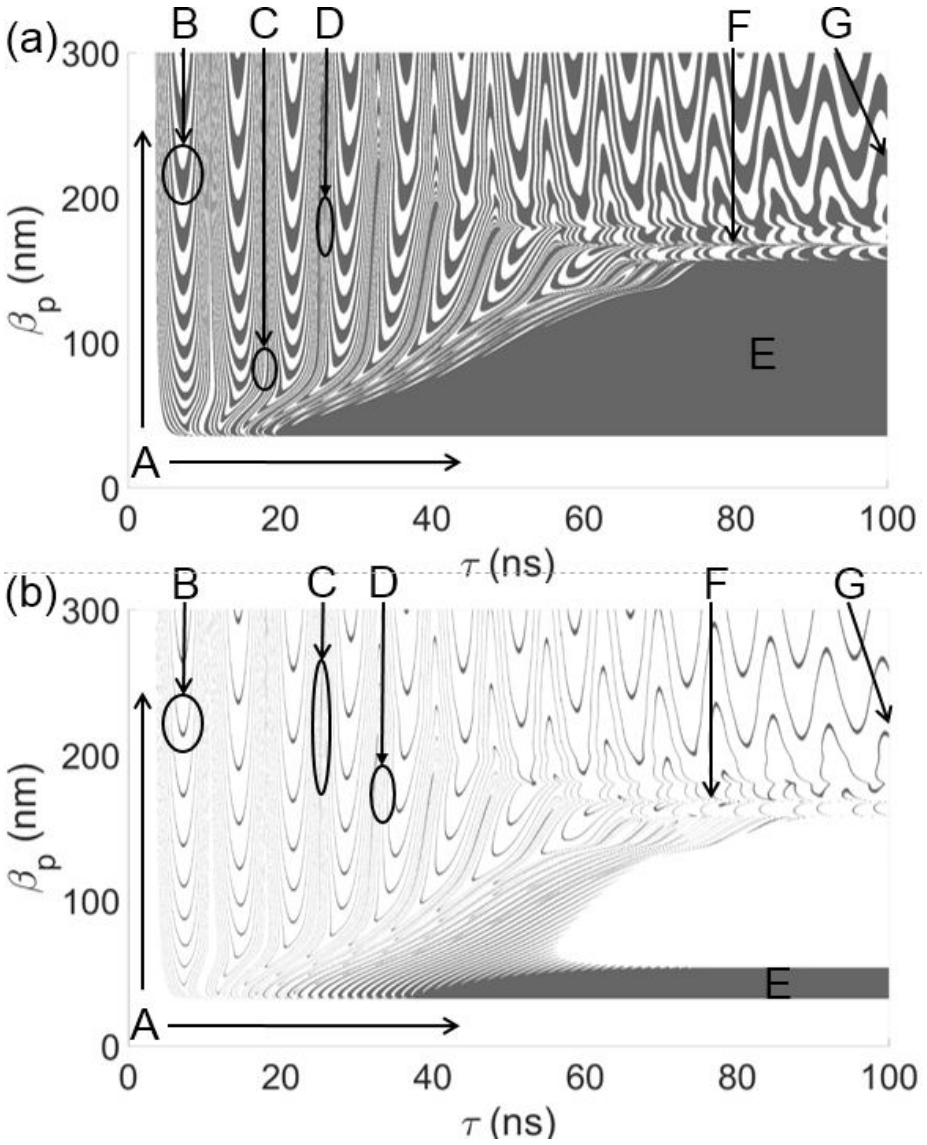

Figure 3: Switching windows for $T = 0$ K. Gray points correspond to pulses that result in successful switching, and white points to pulses that fail to switch. For (a) $\beta_0 = 0$, and for (b) $\beta_0 = -30.5$ nm.

for larger β_p become distorted for β_p in region E. Features for smaller β_p appear to be pulled to the left because the increased steepness of the potential within the pinning sites causes the vortex to precess faster.

Pulses in region G push the vortex beyond the target site so that at long τ it settles into different outer rings of the basins of attraction depending on the

value of β_p, rather than into the target site. The curves are due to the vortex precessing into and out of one of the rings of either basin. For $\tau > 100$ ns (not shown) the vortex would eventually settle while the pulse is still on, and the curves would become horizontal stripes that extend out to $\tau \to \infty$. Finally, region F is similar to region G except that the curves are disjoint, which occurs for $170 \lessapprox \beta_p \lessapprox 180$ nm. In the inset of Fig. 1(a) it can be seen that for these β_p there exist two equilibria x_{eq}. One is the target site, the other lies out beyond the target site at $x \approx 180$ nm. If the vortex approaches the equilibrium that lies beyond the target site then it will be located in a different part of the basins of attraction than if it approaches the target. Thus, in region F, the smooth curves of G are replaced by short, disjoint curves of different widths (in time) as a result of the $x_{eq}(\beta_p)$ the vortex settles into varying discontinuously.

From the basins of attraction maps (Fig. 2), and switching windows (Fig. 3), the deterministic behavior of the vortex during the switching process can be fully explained. This forms the basis for understanding the switching behavior when thermal noise is taken into account.

4. Room temperature vortex dynamics

For nonzero temperature, a stochastic term $\mathbf{F}_s$ (defined by Eqs. 3,4) is added to the equation of motion, making it non-deterministic. When $\mathbf{F}_s \neq \mathbf{0}$, Eq. 2 was solved using the Euler-Maruyama method in MATLAB. [27] In all of these simulations the system was assumed to be at room-temperature. A single solution to Eq. 2 for $T > 0$ K is denoted $\mathbf{x}_s(t;\tau)$, where t ranges from 0 to t_f. In order for the solutions to both converge and agree with the ODE solver in the limit of $T = 0$ K, the time step in all simulations was set to 0.001 ns. Note that t_f is long enough that the dynamics have dampened, but short enough that the vortex is unable to escape from either pinning site due to thermal excitations. Thus, for an individual stochastic path $\mathbf{x}_s$,

$$P_n(\tau) = \begin{cases} 0, \mathbf{x}_s(t_f;\tau) \in B_i \\ 1, \mathbf{x}_s(t_f;\tau) \in B_t \end{cases}$$

and the probability of switching for a given τ can be found by averaging $P_n(\tau)$ over N stochastic paths as $N \to \infty$

$$P(\tau) = \left(\frac{1}{N}\right) \sum_{n=1}^{N} P_n(\tau).$$

For convenience we define
$\mathbf{X}_s(t;\tau) = \{\mathbf{x}_{s,1}(t;\tau), \mathbf{x}_{s,2}(t;\tau), ..., \mathbf{x}_{s,N}(t;\tau)\}$ as a collection of N stochastic paths $\mathbf{x}_s(t;\tau)$ for some pulse length τ. In Fig. 4 several $\mathbf{X}_s(\tau;\tau)$ are plotted for different τ and $N = 100$ as red and blue points over the $\beta_0 = 0$ basins of attraction. $\mathbf{x}_s(\tau;\tau)$ that will eventually fall into the initialization site are colored blue, while those that will land in the target site are colored red. The value of τ is shown next to each $\mathbf{X}_s(\tau;\tau)$, and the black curved lines next to all $\tau \geq 13$ ns show which $\mathbf{x}_s(\tau;\tau)$ belong to which τ.

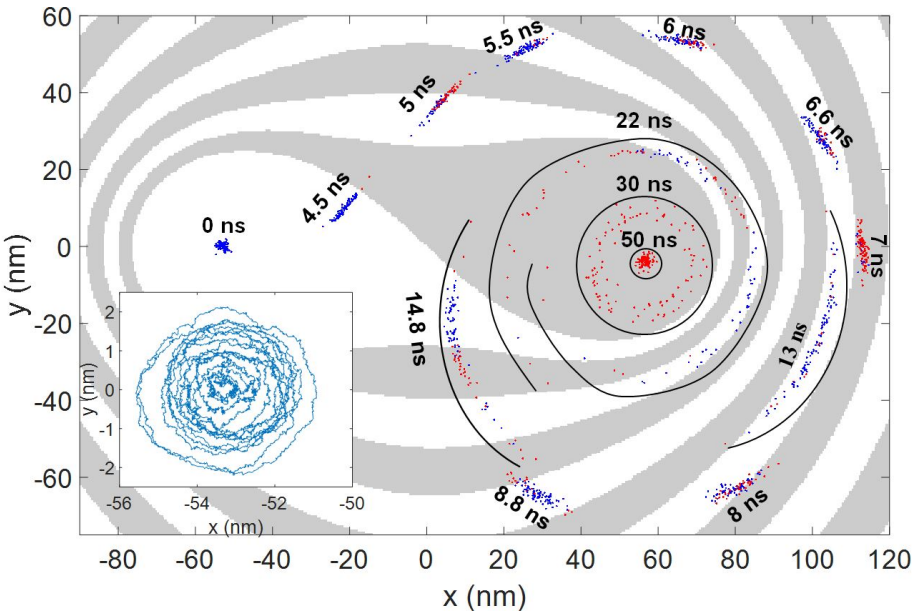

Figure 4: $\mathbf{X}_s(\tau;\tau)$ for $N = 100$ different paths, $\beta_p = 51$ nm, and $\beta_0 = 0$ is plotted for several values of τ. Blue points are $\mathbf{x}_s(\tau;\tau)$ that will fall into the initialization site, and red points are those that will fall into the target site. The inset shows $\mathbf{x}_s(t)$ over 20 ns when the vortex is trapped in the initialization site and $\beta_p = \beta_0 = 0$.

Before the pulse is turned on the vortex is given 1 ms to explore the initialization site under the influence of thermal noise. One $\mathbf{x}_s(t)$ when the vortex was allowed to move around freely within the initialization site for 20 ns is shown in the inset of Fig. 4. In agreement with previous studies [20, 17] (without pinning) it was found that the vortex would undergo spontaneous gyrotropic motion due to thermal excitations when it was started at equilibrium. With 1 ms to explore the initialization site, the standard deviation of the vortex's gyrotropic precession was found to be 1.22 nm given room-temperature thermal fluctuations. This variance in the possible position of the vortex before the pulse turned on was found to be too small to have a significant effect on $P(\tau)$.

From Fig. 4 it can be observed that when the pulse turns off at $t = \tau$ a majority of the different paths $\mathbf{x}_s(\tau;\tau)$ in each $\mathbf{X}_s(\tau;\tau)$ lie in the basin that they will stay in. Within each cluster of $\mathbf{x}_s(\tau;\tau)$, the red dots tend to lie in the target's basin and the blue dots usually lie in the initialization site's basin. The value of $P(\tau)$ can therefore be approximated by looking at the spread in $\mathbf{X}_s(\tau;\tau)$ over the basins of attraction:

$$P_n(\tau) \approx \begin{cases} 0, \mathbf{x}_{s,n}(\tau;\tau) \in B_i \\ 1, \mathbf{x}_{s,n}(\tau;\tau) \in B_t \end{cases}$$

Thus, to understand the effect of thermal fluctuations on $P(\tau)$, the most

important dynamics to consider are those that occur between $t = 0$ and $t = \tau$. Fig. 4 shows that as τ is increased $\mathbf{X}_s(\tau;\tau)$ becomes spread over a larger area, particularly in the direction of motion. This occurs because although each stochastic path $\mathbf{x}_s(t;\tau)$ closely follows the deterministic path $\mathbf{x}_d(t;\tau)$, at any given time in the precession (prior to entering the pinning sites, whereupon the successful and unsuccessful paths diverge) different $\mathbf{x}_s(t;\tau)$ have traveled different distances along $\mathbf{x}_d(t;\tau)$. The evolution of $\mathbf{X}_s(t;\tau)$ for two values of τ can be seen as videos in Fig. 5, which shows that each time $\mathbf{X}_s(t;\tau)$ crosses in between the two pinning sites during its precession it becomes more spread out. This is due to the flatness of the potential in between the two pinning sites (see $-50 < x < 0$ nm in Fig. 1(b)). When $\nabla U \approx \mathbf{0}$ small changes in $\dot{\mathbf{x}}$ due to $\mathbf{F}_s$ produce large changes in $\mathbf{x}$. In Fig. 4, the amount of spread in $\mathbf{X}_s(\tau;\tau)$ can, for instance, be observed to sharply increase between $\tau = 14.8$ ns, where $\mathbf{X}_s(\tau;\tau)$ extends over 4 basin boundaries, and $\tau = 22$ ns, where it lies across 8. It can be expected, then, that the deviation of $P(\tau)$ from the $T = 0$ K case will increase in time as the noise begins to dominate, and $\mathbf{X}_s(\tau;\tau)$ spreads out so much that the basin occupied by $\mathbf{x}_d(\tau;\tau)$ is no longer a good predictor of $P(\tau)$.

[See videos stochastic_paths_tau7.4ns.avi and stochastic_paths_tau14.8ns.avi]

Figure 5: Videos showing the evolution of $\mathbf{X}_s(t;\tau)$ for $\tau = 14.8$ ns and $\tau = 7.4$ ns. In both cases, $\beta_0 = 0$ and $\beta_p = 51$ nm. The basins of attraction for $\beta = 0$ are shown in the background. A black line indicates the $T = 0$ trajectory $\mathbf{x}_d(t;\tau)$ with an asterisk marking the point where the pulse has turned off.

The stochastic paths $\mathbf{X}_s(t;\tau)$ for $t \geq \tau$ become completely dephased as they settle into the pinning sites. Fig. 6(a) displays $\mathbf{X}_s(\tau;\tau)$ for $\tau = 14.8$ ns as red and blue points (which are also plotted in Fig. 4), and red and blue lines for $\mathbf{X}_s(t;\tau)$ for $t > 14.8$ ns over the gray and white basins of attraction map for $\beta_0 = 0$ (see also Fig. 5). Almost every $\mathbf{x}_s(t;\tau)$ can be seen to stay in a single basin as it precesses around and eventually falls into one of the two pinning sites. As a result of $\mathbf{X}_s(\tau;\tau)$ being spread over multiple basin boundaries, different $\mathbf{x}_s(t;\tau)$ enter the pinning sites at different times. This can be observed in the videos in Fig. 5 as well as in Fig. 6(b) and (c), which show $\mathbf{X}_s(t;\tau)$ for $t = 18$ and 24 ns respectively. At $t = 18$ ns, $\mathbf{x}_s(t;\tau)$ that were closest to the pinning sites have already entered them while those that were farther out continue to precess outside of the pinning sites. At $t = 24$ ns, all the $\mathbf{x}_s(t;\tau)$ have entered the pinning sites and continue to precess around the local minima at different distances depending on their position at $t = \tau$.

This dephasing can be observed by plotting the mean $x_{s,n}(\tau;\tau)$ versus τ (black curves in Fig. 7(a) and (b)):

$$x_s(\tau;\tau) = \left(\frac{1}{N}\right) \sum_{n=1}^{N} x_{s,n}(\tau;\tau).$$

By 22 ns $x_s(\tau;\tau)$ has almost completely dephased, while $x_d(\tau;\tau)$, which is plotted in red in Fig. 7(a) and (b), does not settle until ~ 40 ns. The spread

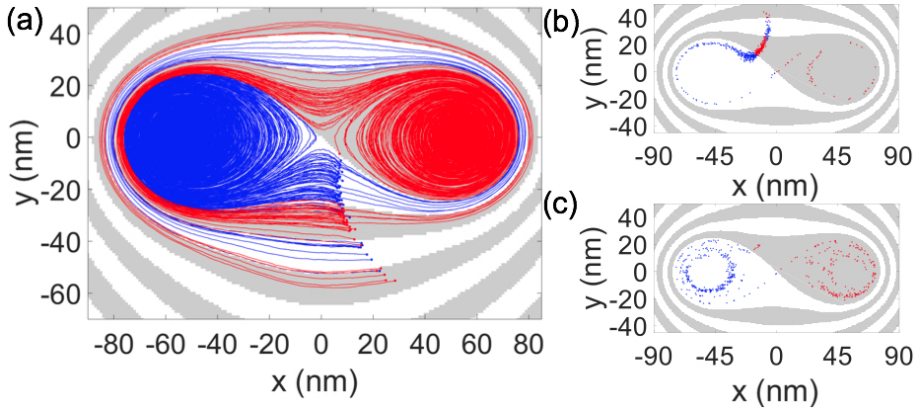

Figure 6: Evolution of $\mathbf{X}_s(t > \tau; \tau)$ over time for $N = 100$ paths, $\beta_p = 51$ nm, $\beta_0 = 0$, and $\tau = 14.8$ ns. Blue paths are $\mathbf{x}_{s,n}(t; \tau)$ that will fall into the initialization site, and red paths are those that will fall into the target site. In (a) t was iterated from 14.8 ns to 50 ns, and the dots correspond to the position of each path at 14.8 ns. In (b) the position of each path at $t = 18$ ns is plotted, and in (c) the position of each at $t = 24$ ns is shown.

in $\mathbf{X}_s(\tau; \tau)$ causes $x_s(\tau; \tau)$ to reach its final value almost 20 ns before $x_d(\tau; \tau)$ does.

5. Simulated switching probability

The probability of switching the vortex between two bistable pinning sites can now be calculated, and the mechanisms behind the experimentally observed features understood. The deterministic switching discussed in section 3, combined with the stochastic dynamics described in section 4, provides us with a model for studying bistable switching. $P(\tau)$ for $T > 0$ K and $\beta_0 = 0$ is plotted in blue in Fig. 7(a).

For $\tau \lessapprox 5$ ns, $P(\tau) = 0$ because this pulse duration is not long enough to break the vortex free from the initialization site. Near local maxima of $x_s(\tau, \tau)$ (denoted by the vertical dashed lines) there is usually a single peak or trough in $P(\tau)$, which occurs because the vortex will often run along a single basin of attraction for a significant range of τ. Near local minima of $x_s(\tau, \tau)$ (denoted by vertical dotted lines) $P(\tau)$ usually has a trough and then a peak immediately after for $\tau \lessapprox 15$ ns, and a single peak if τ is greater. This behavior can be understood from the basins of attraction map (Fig. 2(a)). Minima in $x_s(\tau; \tau)$ occur when $\mathbf{x}_s(\tau; \tau)$ passes in between the two pinning sites during its precession. For the initial passes the vortex first travels through a relatively wide region of B_i, and then immediately after through a wider region of B_t. As τ increases the radius of precession decreases, and the width of B_i that the vortex passes over when it is in between the two pinning sites narrows, while the width of B_t widens. This causes the troughs in $P(\tau)$ near minima in $x_s(\tau; \tau)$ to become narrower and shallower as τ increases until they are drowned out by noise completely and only the peaks are left.

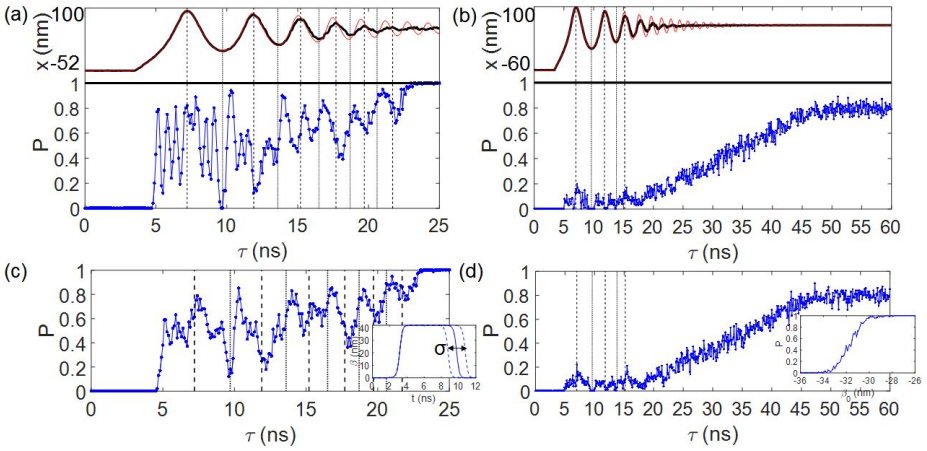

Figure 7: Simulated probability of switching for $\beta_0 = 0$ and $\beta_0 = -30.5$ nm. $P(\tau)$ for $\beta_p = 42$ nm that were averaged over $N = 100$ trials at each τ are plotted in blue, and vertical lines are shown every half-period starting from the first period of the vortex's precession in each sub-figure. (a) $\beta_0 = 0$ and $\sigma = 0$. The black curve shows $x_s(\tau;\tau)$, and the red curve $x_d(\tau;\tau)$ for the same β_0, β_p. (b) $\beta_0 = -30.5$ nm and $\sigma = 0$. The black curve shows $x_s(\tau;\tau)$, and the red curve $x_d(\tau;\tau)$ using the same parameters as were used to simulate $P(\tau)$. (c) is identical to (a) except $\sigma = 0.2$ ns and the inset shows a magnetic field pulse with jitter. It has a height $\beta_p = 42$ nm, and length $\tau = 10$ ns $\pm\sigma = 1$ ns. (d) is the same as (b) but with $\sigma = 0.2$ ns. The inset shows $P(\tau = 50\text{ns})$ versus β_0.

In addition to the oscillations in $P(\tau)$ that occur at the gyrotropic frequency, a steady rise from $P(\tau) \approx 0.5$ at short τ to $P(\tau) = 1$ at long τ can also be observed in Fig. 7(a). This rise is due to the vortex settling into the target site as τ is increased, because as it settles a greater number of $\mathbf{x}_s(\tau;\tau)$ at each τ are located in the target's basin. Once $\tau \gtrapprox 22$ ns, all $\mathbf{x}_s(\tau;\tau)$ lie in the target site and $P(\tau)$ saturates. Finally, there are also very fast oscillations for $\tau \lessapprox 10$ ns that have a half-period of ~ 0.2 ns. These correspond to the vortex quickly cutting in and out of the two basins in between the half-period and period of its precession. For $\tau \gtrapprox 10$ ns these fast oscillations are smeared out by the thermal noise, because after one precession $\mathbf{X}_s(\tau;\tau)$ has become spread out across multiple basin boundaries (see Fig. 4).

$P(\tau)$ for $\beta_0 = -30.5$ nm has dynamics that are similar to the symmetric case, but more suppressed. In Fig. 7(b) $P(\tau)$ is again plotted in blue. It can be observed that the first and third maxima of $x_s(\tau;\tau)$ are near single peaks in $P(\tau)$, while the second maximum is close to a single trough in $P(\tau)$. This can also be observed in the basins of attraction map in Fig. 2(b): during the first and third precession (when the vortex is farthest from the pinning sites) $x_d(\tau;\tau)$ runs along B_t, while during the second precession it runs along B_i instead.

The first minimum of $x_s(\tau;\tau)$ in Fig. 7(b) corresponds to a relatively wide trough in $P(\tau)$. This behavior, as in the symmetric case, can be understood from the basins of attraction map. Near the vortex's point of closest approach to the target site during each precession, it first travels through B_i, and then

through B_t. Due to the disparity in size between the two pinning sites, B_t along $\mathbf{x}_s(\tau;\tau)$ in this region is not large enough for there to be a peak in $P(\tau)$, unlike in the symmetric case.

For τ long enough that the vortex begins to settle into the target site, $P(\tau)$ gradually rises for ~ 30 ns until it saturates. The reason for this gradual rise can be seen in Fig. 4. For long τ, $\mathbf{X}_s(\tau;\tau)$ becomes spread into an approximate circle whose radius decreases as τ continues to increase. Consequently, peaks or troughs in $P(\tau)$ no longer occur near maxima or minima in $x_s(\tau;\tau)$, but instead the noise dominates. Once τ becomes long enough that all $\mathbf{x}_{s,n}(\tau;\tau)$ have fallen into the target site $P(\tau)$ saturates at ~ 0.8.

In order to better understand why $P(\tau)$ for the asymmetric potential does not saturate at 1 we calculated $P(\tau = 50\text{ns})$ as β_0 was varied. P is plotted in blue as the inset of Fig. 7(d). $\tau = 50$ ns was chosen because for $\beta_p = 42$ nm this pulse length is sufficient to ensure that the vortex always settles into the target site before the pulse turns off. For β_0 close to 0 the target site is deep enough that if the vortex has settled then it lacks sufficient energy to escape when the pulse turns off. As β_0 is made more negative the vortex gains more energy when the pulse turns off, and at $\beta_0 \approx -27$ nm the vortex will occasionally break free and settle into the initialization site. As β_0 continues to be made more negative the probability of the vortex remaining in the target site after the pulse turns off decreases until it approaches 0 at $\beta_0 \approx -33$ nm.

A second source of uncertainty besides thermal fluctuations was also taken into account in the simulations. Waveform generators are subject to jitter in the length of the pulses they output. To account for this, we introduced Gaussian white noise to the pulse length that had a standard deviation σ, as illustrated in the inset of Fig. 7(c). It was noted in section 4 that the thermal perturbations can be thought of as adding uncertainty to the position of the vortex on the basins of attraction map when the pulse turns off. Adding noise to the pulse length τ is simply an additional source of uncertainty in the vortex position when the pulse ends, resulting in a greater spread in $\mathbf{X}_s(\tau;\tau)$. Fig. 7(c) is identical to (a) except with $\sigma = 0.2$ ns instead of 0. It can be observed that the peaks and troughs in $P(\tau)$ that occur near the half-period and period of the precession remain, but the fast oscillations for $\tau \lessapprox 10$ ns have been smeared out. Jitter was also included when $\beta_0 = -30.5$ nm, and $P(\tau)$ for $\sigma = 0.2$ ns is shown in blue in Fig. 7(d). It can be seen that for $\tau \lessapprox 20$ ns the peaks and troughs near the half-period and period of the vortex precession stand out more above the background noise compared to $P(\tau)$ in Fig. 7(b) where $\sigma = 0$.

6. Summary

By using the Thiele equation for a massless, rigid vortex we simulated its dynamic motion in a bistable pinning potential when it was subject to thermal fluctuations. In order to understand the process of switching the vortex from one pinning site to the other using a magnetic field pulse, we mapped out the basins of attraction of the two pinning sites. Two bistable potentials were studied, one in which the pinning sites were of the same size (symmetric potential), and

one in which the initialization site was larger than the target site (asymmetric). Peaks and troughs in the probability of switching in both cases were found to generally occur near the half-period and period of the vortex's precession. This was because for pulses close to these times the vortex would be located comfortably inside one of the two basins when the pulse turned off. When thermal noise was added, only pulses with lengths close to the half-period or period could thus result in consistent switching.

For longer pulse lengths the vortex was found to have sufficient time to begin to settle into the target site when the pulse was on. This resulted in a gradual rise in the probability of switching versus pulse length, until the pulse was left on long enough that the vortex had time to completely settle, at which point the probability saturated. The simulations for the asymmetric potential were found to have good qualitative agreement with previous research. [5] Our work suggests that by mapping out the basins of attraction of two bistable pinning sites the probability of successfully switching the vortex between the two sites for different pulse lengths can be well understood. This may prove useful in identifying methods for quickly and reliably switching the vortex between fabricated pinning sites in future magnetic memory devices.

This work was supported by the U.S. Department of Energy, Office of Science, Basic Energy Sciences, under Award #DE-SC008148.

[1] S. S. P. Parkin, M. Hayashi, L. Thomas, Magnetic domain-wall racetrack memory., Science (New York, N.Y.) 320 (5873) (2008) 190–4. doi:10.1126/science.1145799.
URL http://www.sciencemag.org/content/320/5873/190.short

[2] M. Rahm, J. Stahl, D. Weiss, Programmable logic elements based on ferromagnetic nanodisks containing two antidots, Applied Physics Letters 87 (18) (2005) 182107. doi:10.1063/1.2120914.
URL http://aip.scitation.org/doi/10.1063/1.2120914

[3] M. V. G. Dutt, L. Childress, L. Jiang, E. Togan, J. Maze, F. Jelezko, A. S. Zibrov, P. R. Hemmer, M. D. Lukin, Quantum Register Based on Individual Electronic and Nuclear Spin Qubits in Diamond, Science 316 (5829) (2007) 1312–1316. doi:10.1126/science.1139831.
URL http://www.sciencemag.org/cgi/doi/10.1126/science.1139831

[4] M. S. Wolf, R. Badea, J. Berezovsky, Fast, nanoscale addressability of nitrogen-vacancy spins via coupling to a dynamic ferromagnetic vortex, Nature Communications 7 (2016) 5. arXiv:1510.07073, doi:10.1038/ncomms11584.
URL http://www.nature.com/doifinder/10.1038/ncomms11584

[5] R. Badea, M. S. Wolf, J. Berezovsky, Exploiting bistable pinning of a ferromagnetic vortex for nitrogen-vacancy spin control, Applied Physics Letters 109 (13) (2016) 132403. doi:10.1063/1.4963670.
URL http://scitation.aip.org/content/aip/journal/apl/109/13/10.1063/1.4963670

[6] A. Fert, V. Cros, J. Sampaio, Skyrmions on the track, Nature Publishing Group 8. doi:10.1038/nnano.2013.29.
URL https://www.nature.com/nnano/journal/v8/n3/pdf/nnano.2013.29.pdf

[7] R. P. Cowburn, D. K. Koltsov, A. O. Adeyeye, M. E. Welland, D. M. Tricker, Single-Domain Circular Nanomagnets, Physical Review Letters 83 (5) (1999) 1042–1045. doi:10.1103/PhysRevLett.83.1042.
URL http://link.aps.org/doi/10.1103/PhysRevLett.83.1042

[8] T. Shinjo, T., Okuno, T., Hassdorf, R., Shigeto, K., Ono, Magnetic Vortex Core Observation in Circular Dots of Permalloy, Science 289 (5481) (2000) 930–932. doi:10.1126/science.289.5481.930.
URL http://www.sciencemag.org/content/289/5481/930.abstract

[9] R. Höllinger, A. Killinger, U. Krey, Statics and fast dynamics of nanomagnets with vortex structure, Journal of Magnetism and Magnetic Materials 261 (1-2) (2003) 178–189. doi:10.1016/S0304-8853(02)01471-3.
URL http://linkinghub.elsevier.com/retrieve/pii/S0304885302014713

[10] K. Y. Guslienko, V. Novosad, Y. Otani, H. Shima, K. Fukamichi, Field evolution of magnetic vortex state in ferromagnetic disks, Applied Physics Letters 78 (24) (2001) 3848. doi:10.1063/1.1377850.
URL http://scitation.aip.org/content/aip/journal/apl/78/24/10.1063/1.1377850

[11] S. B. Choe, Y. Acremann, A. Scholl, A. Bauer, A. Doran, J. Stöhr, H. A. Padmore, Vortex core-driven magnetization dynamics., Science (New York, N.Y.) 304 (5669) (2004) 420–2. doi:10.1126/science.1095068.
URL http://www.sciencemag.org/content/304/5669/420.shorthttp://www.ncbi.nlm.nih.gov/pubmed/15087545

[12] K. Y. Guslienko, B. A. Ivanov, V. Novosad, Y. Otani, H. Shima, K. Fukamichi, Eigenfrequencies of vortex state excitations in magnetic submicron-size disks, Journal of Applied Physics 91 (10) (2002) 8037. doi:10.1063/1.1450816.
URL http://scitation.aip.org/content/aip/journal/jap/91/10/10.1063/1.1450816

[13] T. Y. Chen, M. J. Erickson, P. A. Crowell, C. Leighton, Surface Roughness Dominated Pinning Mechanism of Magnetic Vortices in Soft Ferromagnetic Films, Physical Review Letters 109 (9) (2012) 097202. doi:10.1103/PhysRevLett.109.097202.
URL https://link.aps.org/doi/10.1103/PhysRevLett.109.097202

[14] J. A. J. Burgess, A. E. Fraser, F. F. Sani, D. Vick, B. D. Hauer, J. P. Davis, M. R. Freeman, Quantitative Magneto-Mechanical Detection and Control of the Barkhausen Effect, Science 339 (6123) (2013) 1051–1054.

doi:10.1126/science.1231390.
URL http://www.sciencemag.org/content/339/6123/1051.short

[15] R. Badea, J. Frey, J. Berezovsky, Magneto-optical imaging of vortex domain deformation in pinning sites, Journal of Magnetism and Magnetic Materials 381 (2015) 463–469. doi:10.1016/j.jmmm.2015.01.036.
URL http://www.sciencedirect.com/science/article/pii/S0304885315000682

[16] R. Compton, P. Crowell, Dynamics of a Pinned Magnetic Vortex, Physical Review Letters 97 (13) (2006) 137202. doi:10.1103/PhysRevLett.97.137202.
URL http://link.aps.org/doi/10.1103/PhysRevLett.97.137202

[17] G. M. Wysin, W. Figueiredo, Thermal vortex dynamics in thin circular ferromagnetic nanodisks, Physical Review B 86 (10) (2012) 104421. doi:10.1103/PhysRevB.86.104421.
URL https://link.aps.org/doi/10.1103/PhysRevB.86.104421

[18] T. Kamppeter, F. G. Mertens, E. Moro, A. Sánchez, A. R. Bishop, Stochastic vortex dynamics in two-dimensional easy-plane ferromagnets: Multiplicative versus additive noise, Physical Review B 59 (17) (1999) 11349–11357. doi:10.1103/PhysRevB.59.11349.
URL https://link.aps.org/doi/10.1103/PhysRevB.59.11349

[19] W. E, W. Ren, E. Vanden-Eijnden, Energy landscape and thermally activated switching of submicron-sized ferromagnetic elements, Journal of Applied Physics 93 (4) (2003) 2275–2282. doi:10.1063/1.1536737.
URL http://aip.scitation.org/doi/10.1063/1.1536737

[20] T. S. Machado, T. G. Rappoport, L. C. Sampaio, Vortex core magnetization dynamics induced by thermal excitation, Applied Physics Letters 100 (11) (2012) 112404. doi:10.1063/1.3694757.
URL http://aip.scitation.org/doi/10.1063/1.3694757

[21] A. A. Thiele, Steady-State Motion of Magnetic Domains, Physical Review Letters 30 (6) (1973) 230–233. doi:10.1103/PhysRevLett.30.230.
URL https://link.aps.org/doi/10.1103/PhysRevLett.30.230

[22] D. L. Huber, Dynamics of spin vortices in two-dimensional planar magnets, Physical Review B 26 (7) (1982) 3758–3765. doi:10.1103/PhysRevB.26.3758.
URL https://link.aps.org/doi/10.1103/PhysRevB.26.3758

[23] G. M. Wysin, Magnetic vortex mass in two-dimensional easy-plane magnets, Physical Review B 54 (21) (1996) 15156–15162. doi:10.1103/PhysRevB.54.15156.
URL https://link.aps.org/doi/10.1103/PhysRevB.54.15156

[24] E. Saitoh, H. Miyajima, T. Yamaoka, G. Tatara, Current-induced resonance and mass determination of a single magnetic domain wall, Nature 432 (7014) (2004) 203–206. doi:10.1038/nature03009.
URL http://www.ncbi.nlm.nih.gov/pubmed/15538364http://www.nature.com/doifinder/10.1038/nature03009

[25] D. Bedau, M. Kläui, S. Krzyk, U. Rüdiger, G. Faini, L. Vila, Detection of Current-Induced Resonance of Geometrically Confined Domain Walls, Physical Review Letters 99 (14) (2007) 146601. doi:10.1103/PhysRevLett.99.146601.
URL https://link.aps.org/doi/10.1103/PhysRevLett.99.146601

[26] K. Y. Guslienko, G. N. Kakazei, J. Ding, X. M. Liu, A. O. Adeyeye, Giant moving vortex mass in thick magnetic nanodots., Scientific reports 5 (2015) 13881. doi:10.1038/srep13881.
URL http://www.ncbi.nlm.nih.gov/pubmed/26355430http://www.pubmedcentral.nih.gov/articlerender.fcgi?artid=PMC4565097

[27] A. Horchler, GitHub SDETools Version 1.3 (2016).
URL https://github.com/horchler/SDETools